Mon. Not. R. Astron. Soc. **0000**, 1–27 (2013) Printed 10 May 2013 (MN LATEX style file v2.2)

Relativistic AGN jets I. The delicate interplay between jet structure, cocoon morphology and jet-head propagation

S. Walg, [1,2⋆] A. Achterberg, [1] S. Markoff, [2] R. Keppens, [3] Z. Meliani [4]
[1]*Astronomical Institute, Radboud University Nijmegen, Heyendaalseweg 135, 6525 AJ Nijmegen, The Netherlands*
[2]*Astronomical Institute "Anton Pannekoek," University of Amsterdam, Science Park 904, 1098 XH Amsterdam, The Netherlands*
[3]*Centre for mathematical Plasma Astrophysics, Department of Mathematics, KU Leuven, Celestijnenlaan 200B, 3001 Heverlee, Belgium*
[4]*LUTH, Observatoire de Paris, France*

10 May 2013

ABSTRACT
Current observations have shown that astrophysical jets reveal strong signs of radial structure. They suggest that the inner region of the jet, the jet spine, consists of a low-density, fast-moving gas, while the outer region of the jet consists of a more dense and slower moving gas, called the jet sheath. Moreover, if jets carry angular momentum, the resultant centrifugal forces lead to a radial stratification. Current observations are not able to fully resolve the radial structure, so little is known about its actual profile. We present three AGN jet models in $2.5D$ of which two have been given a radial structure. The first model is a homogeneous jet, the only model that doesn't carry angular momentum; the second model is a spine-sheath jet with an isothermal equation of state; and the third jet model is a (piecewise) isochoric spine-sheath jet, with constant but different densities for jet spine and jet sheath. In this paper, we look at the effects of radial stratification on jet integrity, mixing between the different jet components and global morphology of the jet-head and surrounding cocoon. We consider steady jets that have been active for 23 Myr. All jets have developed the same number of strong internal shocks along their jet axis at the final time of simulation. These shocks arise when vortices are being shed by the jet-head. We find that all three jets maintain their stability all the way up to the jet-head. The isothermal jet maintains part of its structural integrity at the jet-head where the distinction between jet spine and jet sheath material can still be made. In this case, mixing between jet spine and jet sheath within the jet is fairly inefficient. The isochoric jet, on the other hand, loses its structural jet integrity fairly quickly after the jet is injected. At its jet-head, little structure is maintained and the central part of the jet predominantly consists of jet sheath material. In this case, jet spine and jet sheath material mix efficiently within the jet. We find that the propagation speed for all three models is less than expected from simple theoretical predictions. We propose this is due to an enlarged cross section of the jet which impacts with the ambient medium. We show that in these models, the effective surface area is 16 times as large in case of the homogeneous jet, 30 times as large in case of the isochoric jet and can be up to 40 times as large in case of the isothermal jet.

Key words: Hydrodynamics – Relativistic processes – Intracluster medium – Jets – Numerical methods

1 INTRODUCTION

Astrophysical jets are highly collimated outflows of plasma, generated near a compact object from its accretion disk in accreting systems. Jets on parsec (pc) scales are known to arise from a stellar mass compact object in close binaries, such as a white dwarf (WD), a neutron star (NS) or black hole (BH), while jets on kpc-Mpc scales are associated with active galactic nuclei (AGN), where gas is accreted onto a super massive black hole (SMBH) of $10^6 - 10^{10}\ M_\odot$. In this paper we will only focus on jets arising from super massive black hole systems.

Observations show strong signs that astrophysical jets have a transverse (radial) structure (see for instance Sol, Pelletier & Asseo 1989; Giroletti et al. 2004; Ghisellini, Tavecchio & Chiaberge 2005; Gómez et al. 2008). It has been suggested that most jets consist of two different regions, namely a low-density, fast-moving inner region called the *jet spine*, thought to emerge from a region very close to the BH, and a denser and slower moving outer region called the *jet sheath*, thought to emerge from the inner accretion disk. Numerical simulations of accretion near black holes

⋆ email: s.walg@astro.ru.nl

also show such a radial structure emerging, (e.g. Hardee, Mizuno & Nishikawa 2007; Porth & Fendt 2010). However, the formation, properties and evolution of jet spine and jet sheath are not well understood. In fact, whether the observed radial structure is actually the result of an onderlying spine-sheath jet structure has not been verified by observations.

Large-scale jets are usually divided into two categories, namely FRI and FRII jets (Fanaroff & Riley 1974). The distinction is based on jet/lobe luminosity (at 178 MHz) and radio morphology. FRI jets have low luminosity ($< 10^{41}$ erg s^{-1}) and diffusive jets/radio lobes with no prominent hot spots. FRII jets have a high luminosity ($> 10^{41}$ erg s^{-1}), are generally thought to be more stable and collimated and do have prominent hot spots.

Supersonic and under-dense [1] jets inflate a hot and overpressured cocoon through which shocked jet- and ambient material flows. These jets deposit a large amount of energy into the surrounding medium and will alter their direct environment drastically. This phenomenon ties in closely to the study of *AGN feedback*, the question of how part of the energy produced by AGNs is put back into the intergalactic medium and how this influences galaxy evolution, (e.g. Ciotti & Ostriker 2007; Schawinski et al. 2007; Sijacki et al. 2007; Rafferty, McNamara & Nulsen 2008; Fabian 2012; Gitti, Brighenti & McNamara 2012).

Even though there is strong evidence of a radial structure within AGN jets, the connection between this structure and its impact on the IGM at large scales still remains largely unknown. Since the exact form of a transverse stratification profile might have a large influence on the evolution of the jet at large scales, a study about this aspect is clearly called for.

1.1 Main focus of this research

AGN jets generally remain collimated over huge distances, reaching lengths up to hundreds of kpc or even several Mpc. This implies that these jets either remain very stable internally and are not easily disrupted by instabilities such as the Kelvin-Helmholtz instability, or are confined by external pressure forces.

In this paper, we explore three different jet models, one radially uniform jet (from this point on referred to as the *homogeneous* jet) and two jets with a different type of spine-sheath jet structure. We study the effect of radial stratification on transverse jet integrity and quantify the mixing between jet components in detail. Also, we closely look at the flow patterns that emerge within the jet-head. Moreover, we study how these jets (initiated as typical FRII jets) and their surrounding cocoons have evolved after they have been active for a period of $\sim 10^7$ yr. It is known that a jet and its surrounding cocoon quickly achieve approximate pressure balance as the jet penetrates into the ambient medium. As a result, the jet adapts to pressure variations that travel down the cocoon. We will look in more detail at these pressure waves and how they relate to the formation of strong internal shocks within the jet. Finally, we will compare the actual propagation of the jet-head to the propagation predicted by simple theory.

1.2 Outline of this paper

The outline of this paper is as follows: In Section 2 we present background theory for our models. Then in Section 3 we discuss the method, numerical schemes and the parameter regime. In Section 4 we present the results of the different simulations. Discussion and conclusions are found in Sections 5 and 6.

[1] Compared to the local intergalactic medium (IGM).

2 THEORETICAL BACKGROUND

2.1 Motivation for this research

A number of numerical simulations have been conducted that study the interaction of (relativistic) jets with their ambient medium. These studies include the pure hydrodynamical case (HD), as well as the magnetohydrodynamical case (MHD), with the jet models set up in $2D$, $2.5D$ or $3D$. See for example Marti et al. 1997; Rosen et al. 1999; Aloy et al. 2000; Meliani, Keppens & Giacomazzo 2008; Mignone et al. 2010; Perucho, Quilis & Martí 2011; Bosch-Ramon, Perucho & Barkov 2012; Gilkis & Soker 2012; Prokhorov et al. 2012; Refaelovich & Soker 2012; Soker et al. 2012; Wagner, Bicknell & Umemura 2012. The dependence of the energy feedback from a homogeneous jet to the ambient medium on the finite opening angle of a jet has been studied in detail by Monceau-Baroux, Keppens & Meliani 2012. Moreover, Aloy et al. (2000) have studied jets with a spine-sheath jet structure, however, these jet models do not include angular momentum. They do, however, include magnetic fields.

A global picture of the flow patterns within a jet and its surrounding cocoon has emerged, but a more detailed description of the flow dynamics, and the role of a spine-sheath jet structure in particular is still missing. Having a better understanding of these flow patterns will improve our view on AGN feedback in general. Relevant questions are: How does the jet impact the ambient medium exactly? What part of the ambient medium undergoes strong interaction with the jet and what part is merely deflected? How much mixing is there between shocked ambient medium and shocked jet material? What effect will a different radial stratification have on the jet integrity and possibly the formation and development of internal shocks? And in the case of structured jets, how does spine and sheath material mix internally within the jet, as well as in their surrounding cocoon?

Having a better understanding of the interplay between jet, cocoon and ambient medium, as well as the effect of radial stratification on jet integrity and mixing effects could help us to search for and compare with observational features.

2.2 Jet models

When dealing with jets, it is convenient to express their length scales in terms of the gravitational radius of the black hole in the 'central engine' that feeds jet activity, $R_{\rm g} = GM_{\rm BH}/c^2$, with G the gravitational constant and c the speed of light [2].

Theoretical considerations together with some observational evidence (e.g. Hada et al. 2011) point at a situation where jets in general have distinct regions, characterized by processes that take place at different distances from the central engine. If the jet launching mechanisms for black hole binaries (BHBs) and AGNs are intrinsically similar, then we expect the processes that take place along the jet axis to be approximately scale invariant. In that case, these characteristic regions are located at approximately the same distance, when measured in units of the black hole gravitational radius $R_{\rm g}$. Lobanov (2011) discusses five such distinct regions. VLBI

[2] To give a sense for the dimensions, the gravitational radius for a black hole with $M_{BH} = 10^8 M_\odot$ is $R_{\rm g} \sim 1.48 \times 10^8$ km ≈ 1 AU.

observations of AGNs usually probe the collimation and acceleration region, which occurs at a distance of about $\sim 10^3\ R_{\rm g}$, where magnetic fields are still thought to play a significant role. In some cases, VLBI observations of AGN jets are able to resolve up to even much smaller distances from the central engine (in Hada et al. 2011, M87 is observed only a few tens of gravitational radii from the central engine and recently Doeleman et al. 2012 have been able to resolve the jet base and estimate this region to lie at a distance of $\sim 5.5\ R_{\rm g}$ from the supermassive black hole). However, in our simulations we will focus on the kinetic energy flux dominated (KFD) region of the jets, which typically occurs at $\sim 10^6 - 10^{11}\ R_{\rm g}$. There, the magnetic field is weak, so it doesn't significantly affect the dynamics of the jet flow [3]. Therefore, we will not be primarily concerned with the dynamical effect of magnetic fields.

It is often assumed that a hot and tenuous plasma is present in the innermost regions of accretion, close to the BH horizon and the innermost stable circular orbit, with magnetic field lines threading the BH horizon. If the BH is spinning, gas and magnetic field lines are carried along by a general relativistic effect called 'frame dragging', extracting angular momentum from the spinning BH (Blandford & Znajek 1977). It is therefore expected that if jets indeed consist of a spine-sheath jet structure, the jet spine emerges from this region, and consists of a hot, tenuous and fast-rotating gas.

Further out, but still within the inner accretion disk, material is thought to be less hot and more dense, rotating at lower velocities than material in the direct vicinity of the BH. The jet sheath is likely to emerge from this region (Blandford & Payne 1982). Therefore, it is expected that the jet sheath consists of a denser and colder flow, with lower azimuthal velocities than the jet spine. At large distances from the central engine, the jet sheath material still has a relativistic bulk velocity, but a lower Lorentz factor than that of the jet spine. For work relating radiative features of AGN jets to a spine-sheath jet configuration, see for instance Ghisellini et al. (2005).

In this paper we consider both a homogeneous jet with constant density and pressure over its cross section, as well as jets with a spine-sheath jet configuration. It should be noted that not much is known about the actual radial structure of a spine-sheath jet, so we will assume that all jets start out in pressure equilibrium with their ambient medium. We consider two different types of structured jets: The first model uses a polytropic index $\Gamma = 5/3$ and is piecewise isochoric: a constant but different density for jet spine and jet sheath, which we will refer to as the *isochoric jet* from now on. The other model is set up with an isothermal equation of state and assumes a constant temperature across the jet cross section. We will refer to this model as the *isothermal jet* from now on. These two cases result in a different radial structure, as will be discussed in section 2.4. Jet spine and jet sheath are given different values for density, pressure and velocity, and we allow for rotation around the jet axis, so that the jet carries angular momentum.

2.3 Hydrodynamics: basic equations and methods

We have simulated the different jet models making use of the special relativistic, grid-adaptive magneto-hydrodynamical code MPI-AMRVAC (Keppens et al. 2012). In classical and relativistic ideal hydrodynamics, total mass, momentum and energy are conserved. That means that the fundamental equations can be cast in conservative form, which in a 3+1 formulation read:

$$\frac{\partial U_i}{\partial t} + \nabla \cdot \boldsymbol{F}_i = 0\ . \tag{1}$$

Here the U_i (with $i = 1 - 5$) are the conservative variables, and the $\boldsymbol{F_i}$ their corresponding fluxes. These relations can be derived from the covariant formulation, and in particular from the vanishing divergence of the energy-momentum tensor, see for instance Weinberg (1972), Ch. 2.10. Employing units with $c = 1$ from here on, the conservative variables employed in MPI-AMRVAC are defined as:

$$U = \begin{pmatrix} D \\ \boldsymbol{S} \\ \tau \end{pmatrix} \equiv \begin{pmatrix} \gamma\rho \\ \gamma^2\rho h \boldsymbol{v} \\ \gamma^2\rho h - P - \gamma\rho \end{pmatrix}. \tag{2}$$

Here ρ is the mass density in the jet rest frame, $\boldsymbol{v}$ is the velocity vector and $\gamma = 1/\sqrt{1-|\boldsymbol{v}|^2}$ the associated Lorentz factor (proper speed: $\gamma\boldsymbol{v}$). The vector $\boldsymbol{S}$ is the momentum density, P is the pressure and τ is the kinetic energy density that includes the kinetic energy of the bulk and thermal motion [4]. The (relativistic) specific enthalpy h is: [5]

$$h = \frac{e+P}{\rho}\ , \tag{3}$$

with $e = e_{\rm th} + \rho$, the total internal energy density, including the thermal energy density $e_{\rm th}$ and the contribution of the rest-mass energy ρ. Moreover, P is the gas pressure and Γ is the polytropic index of the gas. The corresponding fluxes are:

$$\boldsymbol{F} = \begin{pmatrix} D\boldsymbol{v} \\ \boldsymbol{S}\,\boldsymbol{v} + P\,\mathbf{I} \\ (\tau + P)\boldsymbol{v} \end{pmatrix}, \tag{4}$$

with $\mathbf{I}$ the 3×3 identity matrix.

In order to obtain a complete description of the relativistic fluid, the system is closed with an equation of state (EOS), relating gas pressure to mass density. Instead of simply putting $\Gamma \equiv \mathrm{d}\ln P/\mathrm{d}\ln\rho$ equal to $5/3$ (for a classical ideal gas), or $4/3$ (for a relativistically hot ideal gas), we employ the same interpolation function that was used in Meliani et al. (2008), describing a realistic transition between a relativistically hot gas and a 'cold' non-relativistic gas. This interpolation function is called the Mathews approximation (Blumenthal & Mathews 1976) and is based on the Synge EOS (Synge 1957). The Mathews approximation uses an effective polytropic index equal to:

$$\Gamma_{\rm eff} = \tfrac{5}{3} - \tfrac{1}{3}\left[1 - \left(\frac{\rho}{e}\right)^2\right]. \tag{5}$$

With this definition for the effective polytropic index, the relativistic specific enthalpy can be written as:

$$h = \tfrac{1}{3}\left[4\frac{e}{\rho} - \frac{\rho}{e}\right], \tag{6}$$

and the corresponding closure relation following from (3) becomes:

$$P = \tfrac{1}{3}\left(e - \frac{\rho^2}{e}\right). \tag{7}$$

The total internal energy of the gas per particle is $\epsilon = e/n$, with n the number density of the gas. For a plasma consisting of protons, as is the case for a hadronic jet, the rest-mass energy per particle is $m_{\rm p}$ and the thermal energy of the gas per particle is $\epsilon_{\rm th} = e_{\rm th}/n$. Not

[3] The magnetic field in the KFD region does of course induce the observed synchrotron emission.

[4] Or equivalently, τ is the total energy density in the lab-frame, with the lab-frame rest-mass energy $\gamma\rho$ subtracted.

[5] The quantity ρh is referred to as relativistic enthalpy.

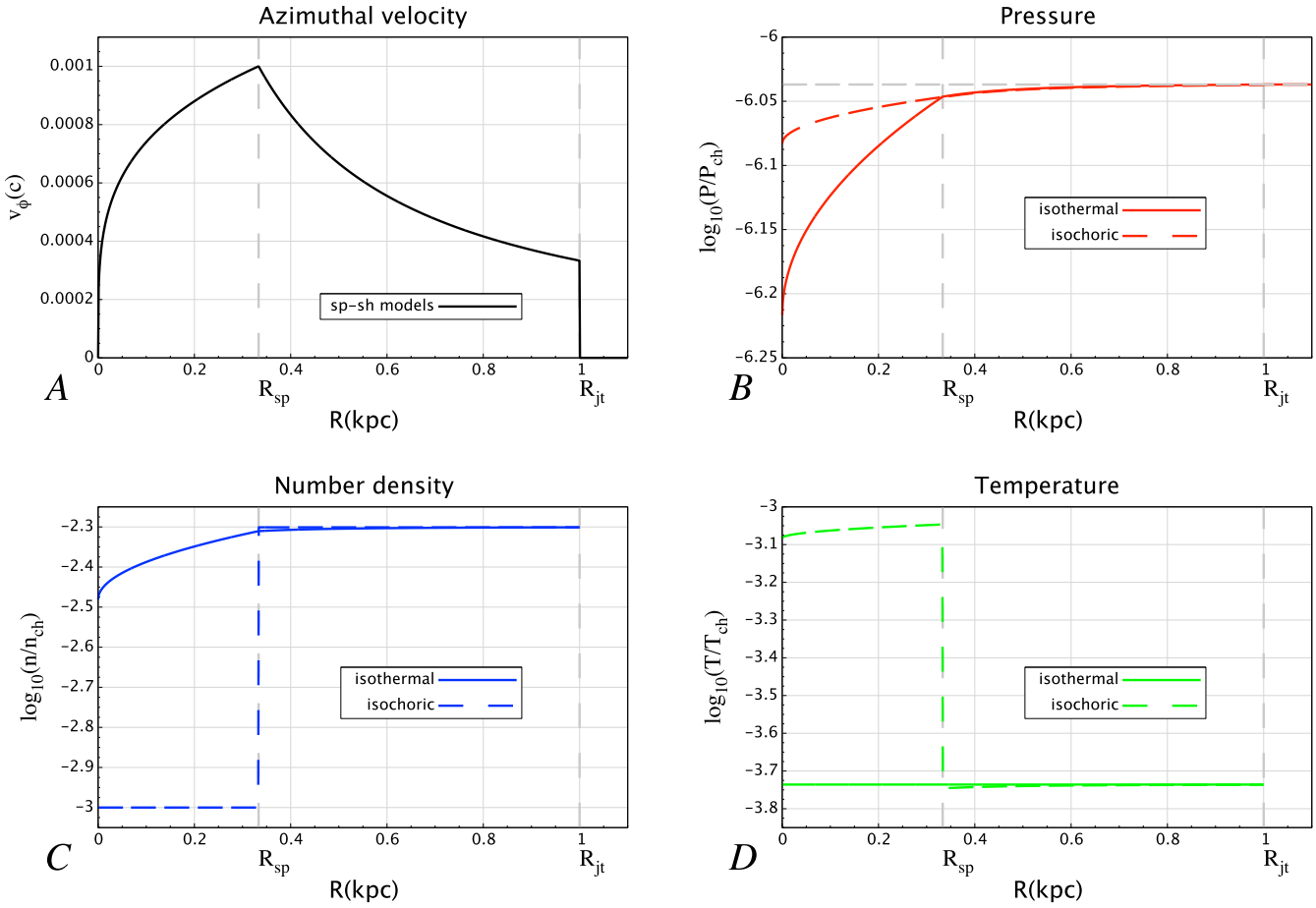

Figure 1. Initial transverse jet profiles for the isothermal jet (solid lines) and the piecewise isochoric jet (dashed lines), in case $V_\phi = 1.0 \times 10^{-3} c$. The cross cuts show in *black* the profile of azimuthal rotation $v_\phi(R)$ (figure **A**). This rotation profile has been used for both the isothermal and the isochoric jet model; In *red*, the $\log_{10}$ of the pressure P in units of the characteristic pressure $P_{ch} = 1.50 \times 10^{-6}$ erg cm^{-3} (figure **B**); In *blue* the $\log_{10}$ of the number density n in units of the characteristic number density $n_{ch} = 10^{-3}$ cm^{-3} (figure **C**); and in *green* the $\log_{10}$ of the thermal temperature T in units of the characteristic temperature $T_{ch} = 1.09 \times 10^{13}$ K (figure **D**) of the jet. In addition, the images show the jet radius at $R_{jt} = 1$ kpc and the jet spine radius at $R_{sp} = R_{jt}/3$ as the two vertical dashed lines. The pressure of the ambient medium is denoted by the dashed horizontal line in figure **B**.

much is known about the composition of an AGN jet at kpc scales. The plasma might consist of electrons and positrons (see for example Reynolds et al. 1996 or Wardle et al. 1998), but it might also be an electron-proton plasma, or a mixture of both. We will however assume that at the length scales we are considering, a significant amount of mixing with the ambient medium has taken place, so that the jet can effectively be described by a hadronic plasma.

It can easily be seen that the effective polytropic index for a non-relativistically 'cold' gas with $\epsilon_{th} << m_p$ reduces to $\Gamma_{eff} = 5/3$, while for a relativistically hot gas with $\epsilon_{th} >> m_p$, it reduces to $\Gamma_{eff} = 4/3$ [6]. See Meliani et al. (2008) for a more complete description of the Mathews approximation to the Synge equation of state.

2.4 Radial pressure profile for spine-sheath jets

Since AGN jets remain collimated over huge distances, they are expected to be in approximate pressure equilibrium with their surroundings. In fact, if a jet does not start out in pressure equilibrium, unbalanced pressure forces at its jet-ambient medium interface cause the jet to either expand, or contract until approximate pressure equilibrium is reached. The question of *how* this ambient medium is defined exactly is less clear. In the "standard model" for double radio galaxies (e.g. Blandford & Rees 1974; Scheuer 1974; Leahy, Muxlow & Stephens 1989; Begelman & Cioffi 1989; Daly 1990), under-dense jets at larger distances from the central engine create a strong bow-shock. This bow-shock encloses a hot and over-pressured cocoon (compared to the undisturbed ambient medium). Since we do not know the exact conditions for such cocoons when we start our simulations, we set the jets up in direct pressure equilibrium with the undisturbed *ambient* intergalactic medium, which we will indicate with a subindex "am" from now on.

In case of the radially uniform, or *homogeneous* jet (which we call case *H*), we set the pressure equilibrium up by equating the jet pressure to the pressure of the ambient medium. For jets with a *spine-sheath jet structure* on the other hand (which we call case *A* for the isochoric jet and case *I* for the isothermal jet), the pressure profile is not trivial. It can be obtained by solving the special rela-

[6] For an electron-positron plasma, the energies at which the gas would become relativistic are lower by a factor $m_e/m_p \sim 5 \times 10^{-4}$.

tivistic hydrodynamic (SRHD) radial force equation that balances the radial pressure force with the centrifugal force due to the rotation of the fluid. We use cylindrical coordinates $(R\ ,\ \phi\ ,\ z)$ with the jet axis along the z-axis and neglect the lateral expansion of the jet (assumed to be slow so that $v_R \ll v_z$) so that the velocity is $\boldsymbol{v} = \left(0\ ,\ v_\phi\ ,\ v_z\right)$. One has:

$$\frac{\mathrm{d}P}{\mathrm{d}R} = \frac{\rho h\, \gamma^2 v_\phi^2}{R} = \frac{\rho h v_\phi^2}{\left(1 - v_z^2 - v_\phi^2\right) R}\ . \tag{8}$$

In this paper, the index "sp" refers to variables and constants belonging to the jet spine, whereas the index "sh" refers to variables and constants belonging to the jet sheath. An analytical solution for the SRHD radial force balance equation can be found if one assumes a self-similar rotation profile of the form:

$$v_\phi^2(R) = \begin{cases} V_{\phi,\mathrm{sp}}^2 \left(\dfrac{R}{R_{\mathrm{sp}}}\right)^{a_{\mathrm{sp}}} & \text{jet spine: } 0 \leqslant R \leqslant R_{\mathrm{sp}}\ , \\ \\ V_{\phi,\mathrm{sh}}^2 \left(\dfrac{R}{R_{\mathrm{sp}}}\right)^{a_{\mathrm{sh}}} & \text{jet sheath: } R_{\mathrm{sp}} < R \leqslant R_{\mathrm{jt}}\ . \end{cases} \tag{9}$$

The same profile is used in Meliani & Keppens (2009). Here R_{sp} is the radius of the jet spine and R_{jt} is the outer radius of the jet sheath, which coincides with the jet radius. $V_{\phi,\mathrm{sp}}$ is a constant that gives the maximum rotation within the jet spine for $R \longrightarrow R_{\mathrm{sp}}$, and similarly for the constant $V_{\phi,\mathrm{sh}}$. The constants a_{sp} and a_{sh} are self-similarity constants. It can be seen immediately that the constant a_{sp} needs to be positive in order to avoid singularities at $R \longrightarrow 0$. Furthermore, the Rayleigh criterion for stability of flows rotating on a cylinder against axisymmetric perturbations is:

$$\frac{\mathrm{d}}{\mathrm{d}R}\left(\gamma h R v_\phi\right) > 0\ , \tag{10}$$

see for instance Pringle & King (2007), Ch. 12. From this it follows that both self-similarity constants need to satisfy the condition $a_{\mathrm{sp}} > -2$ and $a_{\mathrm{sh}} > -2$. We set $a_{\mathrm{sh}} = -2$, corresponding to a jet sheath flow with constant specific angular momentum: $\lambda \equiv \gamma h R v_\phi = \text{constant}$, making it marginally stable according to Rayleigh's criterion. As the self-similarity constant of the jet spine needs to be positive, we adopt the same value that was used in Meliani & Keppens (2009) and set $a_{\mathrm{sp}} = 1/2$.

We solve the radial force-balance equation (8) for two different kinds of jets. The first jet is given constant, but different density for jet spine and jet sheath. There, we set up the radial pressure profile of the jet making use of a polytropic index equal to $\Gamma = 5/3$. The second kind of jet is the isothermal jet where we fix the temperature of the jet by adjusting the density accordingly to the varying pressure, and initializing the jet according to $\Gamma = 1$. Figure 1 shows the initial transverse (radial) profiles of the azimuthal velocity, pressure, number density and temperature that were used in these simulations. In the following sections (2.4.1 and 2.4.2), the actual radial pressure profiles will be derived. The choice for the parameters of jet and ambient medium that have been used to generate the exact jet profiles are discussed in sections 2.5 and 3.

2.4.1 *Pressure profile for the isothermal jet (I)*

To solve the radial force balance equation for the isothermal jet, we first use the ideal gas law to write (8) as:

$$s^2 \frac{dP}{P} = \frac{v_\phi^2 dR}{(1 - v_z^2 - v_\phi^2)R}, \tag{11}$$

where the isothermal sound speed in a relativistic gas s is given by:

$$s^2 = \frac{\mathcal{R}T}{\mu h}, \tag{12}$$

with $\mathcal{R}$ the gas constant and μ the particle mass in units of hydrogen mass. The temperature is taken constant. To solve the radial force balance equation, the temperature for the jet spine and the jet sheath does not necessarily have to be the same. However, we adopt a constant T across jet spine and jet sheath here, where we assume that any differences in temperature have been washed out at large distances from the central engine. We will assume the vertical component of the velocity to be constant $v_z = V_z$ (also not necessarily the same for jet spine and jet sheath) and use the self similar azimuthal velocity profile (9). In that case the pressure profile is easily integrated to:

$$P = A\left\{1 - \alpha\left(\frac{R}{R_{\mathrm{sp}}}\right)^a\right\}^{-\sigma}\ . \tag{13}$$

Here, A, a, α and σ are all constants with the latter three given in the jet spine by:

$$a = a_{\mathrm{sp}}\ \ ,\ \ \alpha_{\mathrm{sp}} = \frac{V_{\phi,\mathrm{sp}}^2}{1 - V_{z,\mathrm{sp}}^2}\ \ ,\ \ \sigma_{\mathrm{sp}} = \frac{1}{a_{\mathrm{sp}} s_{\mathrm{sp}}^2}\ . \tag{14}$$

Expressions in the jet sheath are analogous and can be found by changing the subscript sp $\longrightarrow$ sh. The constant A_{sp} in the jet spine and the corresponding constant A_{sh} in the jet sheath follow from requiring [1] pressure balance at the jet spine-sheath interface at $R = R_{\mathrm{sp}}$ and [2] requiring pressure balance with the pressure P_{am} of the surrounding medium at the jet outer radius $R = R_{\mathrm{jt}}$.

This leads to two conditions:

$$\begin{aligned} A_{\mathrm{sp}}\ \left\{1 - \alpha_{\mathrm{sp}}\right\}^{-\sigma_{\mathrm{sp}}} &= A_{\mathrm{sh}}\ \left\{1 - \alpha_{\mathrm{sh}}\right\}^{-\sigma_{\mathrm{sh}}}\ , \\ A_{\mathrm{sh}}\ \left\{1 - \alpha_{\mathrm{sh}}\left(\frac{R_{\mathrm{jt}}}{R_{\mathrm{sp}}}\right)^{a_{\mathrm{sh}}}\right\}^{-\sigma_{\mathrm{sh}}} &= P_{\mathrm{am}}\ . \end{aligned} \tag{15}$$

These two relations determine A_{sp} and A_{sh}. Moreover, the pressure at the centre of the jet $P(R = 0) = P_0$ also determines the constant A_{sp} by:

$$A_{\mathrm{sp}} = P_0\ . \tag{16}$$

The requirement for the pressure to remain positive throughout the jet's cross section is satisfied when $\alpha_{\mathrm{sp}} < 1$ and $\alpha_{\mathrm{sh}} < 1$, which leads to the physically obvious condition $V_z^2 + V_\phi^2 < 1$, the total speed at the interfaces must be less than the speed of light.

2.4.2 *Pressure profile for the piecewise isochoric jet (A)*

Instead of assuming a constant temperature $T \propto P/\rho$, we now assume a piecewise isochoric (or constant density) jet with in the jet spine a density ρ_{sp}, polytropic index Γ_{sp} and speed $v_z = V_{z,\mathrm{sp}}$, and similarly ρ_{sh}, Γ_{sh} and $V_{z,\mathrm{sh}}$ in the jet sheath. Then the radial force balance equation (8) can be rewritten as:

$$R\,\frac{\mathrm{d}\tilde{P}}{\mathrm{d}R} - \frac{\Gamma}{\Gamma - 1}\,\frac{v_\phi^2}{\left(1 - v_z^2 - v_\phi^2\right)}\,\tilde{P} = 0\ . \tag{17}$$

Here

$$\tilde{P}(R) \equiv \frac{\Gamma - 1}{\Gamma}\,\rho h = P(R) + \frac{\Gamma - 1}{\Gamma}\,\rho\ . \tag{18}$$

Using rotation profile (9) one can solve this equation:

$$\tilde{P}(R) = \tilde{A}\ \left\{1 - \alpha\ \left(\frac{R}{R_{\rm sp}}\right)^{a}\right\}^{-\tau}\ . \tag{19}$$

Here a and α have the same meaning as in the isothermal case. The constant $\tilde{A}$ is determined from requiring pressure equilibrium at the interfaces $R_{\rm sp}$ and $R_{\rm jt}$, as was required in the isothermal case. Moreover, τ is a constant, which for the jet spine is given by:

$$\tau_{\rm sp} = \frac{\Gamma_{\rm sp}}{a_{\rm sp}(\Gamma_{\rm sp} - 1)}\ . \tag{20}$$

As before, expressions in the jet sheath are analogous to the expressions in the jet spine and can be found by changing the subscript sp $\longrightarrow$ sh. The constant $\tilde{A}_{\rm sp}$ in jet spine (and the corresponding constant $\tilde{A}_{\rm sh}$ in the jet sheath) in this case are determined by solving:

$$\begin{aligned}
&\tilde{A}_{\rm sp}\ \left\{1 - \alpha_{\rm sp}\right\}^{-\tau_{\rm sp}} - \frac{\Gamma_{\rm sp} - 1}{\Gamma_{\rm sp}}\,\rho_{\rm sp}\ = \\
&\tilde{A}_{\rm sh}\ \left\{1 - \alpha_{\rm sh}\right\}^{-\tau_{\rm sh}} - \frac{\Gamma_{\rm sh} - 1}{\Gamma_{\rm sh}}\,\rho_{\rm sh}\ , \\
&\tilde{A}_{\rm sh}\ \left\{1 - \alpha_{\rm sh}\left(\frac{R_{\rm jt}}{R_{\rm sp}}\right)^{a_{\rm sh}}\right\}^{-\tau_{\rm sh}}\ =\ P_{\rm am} + \frac{\Gamma_{\rm sh} - 1}{\Gamma_{\rm sh}}\,\rho_{\rm sh}\ .
\end{aligned} \tag{21}$$

These two relations determine $\tilde{A}_{\rm sp}$ and $\tilde{A}_{\rm sh}$, with the constraint that physically allowed solutions must have $P_0 \geqslant 0$, or equivalently:

$$\tilde{P}_0\ =\ \tilde{A}_{\rm sp} \geqslant \frac{\Gamma_{\rm sp} - 1}{\Gamma_{\rm sp}}\,\rho_{\rm sp}\ . \tag{22}$$

2.5 Jet properties: density ratio and kinetic luminosity

Observations of AGN jets yield a few basic parameters, such as the jet length and diameter, the luminosity of jets, lobes and (in FRII sources) hot spots and possibly the synchrotron age based on the observed spectrum of the non-thermal radiation. In addition, it is possible to derive cocoon parameters from the X-ray cavities observed around some of the stronger sources. In principle one can estimate the advance speed of the jet from these data and, using a model, get clues on jet composition, e.g. the question of an electron-positron jet plasma vs. a hydrogen plasma.

In this section we will explain how observed data can be used to calculate the mass density ratio between jet material and material of the ambient medium. Then in section 2.6, we will use this to estimate the jet-head advance speed for a radially uniform jet.

In order to do so, we first define the kinetic luminosity of a jet $L_{\rm jt}$ as the total power $L_{\rm tot}$ that is produced by the jet, with its rest mass energy discharge through the jet subtracted. Still working in units where $c = 1$:

$$L_{\rm jt} = L_{\rm tot} - \dot{M}. \tag{23}$$

The total power $L_{\rm tot}$ for a radially uniform jet is given by:

$$L_{\rm tot} = A_{\rm jt}^2 n_{\rm jt} m_{\rm jt} h_{\rm jt} \gamma_{\rm jt}^2 v_{\rm jt}, \tag{24}$$

and the rest mass energy discharge through the jet $\dot{M}$ by:

$$\dot{M} = A_{\rm jt}^2 n_{\rm jt} m_{\rm jt} \gamma_{\rm jt} v_{\rm jt}. \tag{25}$$

Here $A_{\rm jt} = \pi R_{\rm jt}^2$ is the cylindrical radial cross section of the jet, $n_{\rm jt}$ is the number density of the jet material, $m_{\rm jt}$ is the averaged mass of the particles in the jet and $h_{\rm jt}$ is the specific relativistic enthalpy of the jet material, see eq. (3). Therefore, the kinetic luminosity of a radially uniform jet can be written as:

$$L_{\rm jt} = A_{\rm jt} n_{\rm jt} m_{\rm jt} \gamma_{\rm jt} v_{\rm jt} (h_{\rm jt}\gamma_{\rm jt} - 1). \tag{26}$$

In case of a structured spine-sheath jet, we approximate its kinetic luminosity by adding the contributions from the jet spine and the jet sheath to the kinetic luminosity separately:

$$L_{\rm jt} = L_{\rm sp} + L_{\rm sh}, \tag{27}$$

where $L_{\rm sp}$ and $L_{\rm sh}$ are defined in the same way as (26), but with their indices referring to the corresponding components. In the rest of this derivation we will just focus on the case of the radially uniform, homogeneous jet.

Now suppose that we know the following jet parameters from observations for a particular AGN jet: kinetic luminosity, jet radius and jet velocity (or equivalently a Lorentz factor $\gamma_{\rm jt}$). Suppose that we can also determine a number density $n_{\rm am}$ and temperature $T_{\rm am}$ of the ambient medium (from which we can derive the ambient medium pressure $P_{\rm am}$ with the ideal gas law). With these parameters it is possible to calculate the density ratio between jet material and ambient medium.

First we assume pressure equilibrium at the interface between jet and ambient medium. Then, using equations (3) and (26), one can show that the ratio of number density can be written as:

$$\frac{n_{\rm jt}}{n_{\rm am}} = \frac{(\Gamma - 1)\left(\dfrac{L_{\rm jt}}{\pi R_{\rm jt}^2 n_{\rm am} m_{\rm jt}}\right) - \Gamma\gamma_{\rm jt}\sqrt{\gamma_{\rm jt}^2 - 1}\left(\dfrac{k_{\rm b} T_{\rm am}}{m_{\rm jt}}\right)}{(\Gamma - 1)(\gamma_{\rm jt} - 1)\sqrt{\gamma_{\rm jt}^2 - 1}}, \tag{28}$$

with $k_{\rm b}$ the Boltzmann constant.

As we mentioned before, we assume the jet to be hadronic, so that the number density ratio can be written as a (proper) mass density ratio, given by: [7]

$$\eta_{\rm R} = \frac{\rho_{\rm jt}}{\rho_{\rm am}} = \frac{n_{\rm jt}}{n_{\rm am}}. \tag{29}$$

Jets with $\eta_{\rm R} < 1$ are called *under-dense* and jets with $\eta_{\rm R} > 1$ are called *over-dense*. Under-dense jets are less stable than over-dense jets and develop internal (diamond-shaped) shocks more easily. For under-dense jets the propagation speed of the jet's head is much lower than the velocity of the bulk material of the jet (see section 2.6). For these jets, at the jet's head the jet flow is terminated by a strong shock called the Mach disk.

The intergalactic medium (IGM) in the vicinity of galaxies and inside clusters of galaxies (the so-called intra-cluster medium, or ICM) is usually denoted as a warm-hot intergalactic medium (WHIM). In these regions number densities range from $\sim 5 \times 10^{-6}$ cm^{-3} to $\sim 10^{-3}$ cm^{-3} and temperatures are on the order of $10^5 - 10^7$ K (see e.g. Davé et al. 2001; Davé et al. 2010 and Kunz et al. 2011).

Since many powerful AGN jets are formed inside clusters of galaxies (e.g. Begelman, Blandford & Rees 1984; Smith et al. 2002), we choose to focus on the intra-cluster medium as the ambient medium for our jets and take for the number density $n_{\rm am} = 1 \times 10^{-3}$ cm^{-3} and fix the temperature of the ambient medium to $T_{\rm am} = 10^7$ K.

For the jet we will take a powerful radio source, with a luminosity of $L_{\rm jt}$ = a few $\times\, 10^{46}$ erg s^{-1} (a typical luminosity for FRII and BL Lac sources, see for instance Ito et al. 2008 or Ma et al. 2008). Also, the bulk material of the jets in our simulations is cold (by which we mean that the gas satisfies a classical equation of

[7] Note that the inertia of the material in the lab frame scales as $\gamma^2 nm$ for a given particle mass m.

state, $\Gamma = 5/3$). We will take for the radius of the jet $R_{\rm jt} = 1$ kpc, corresponding to a jet with a typical half-opening angle of 1° (Pushkarev et al. 2009) at a distance of 57 kpc from the central engine [8]. And finally we will take this jet to be trans-relativistic with a moderate Lorentz factor of $\gamma_{\rm jt} = 3$.

Substituting these values into (28) we find a mass density ratio on the order of $\eta_{\rm R} \sim 10^{-3}$, corresponding to very under-dense jets. Table 1 shows the exact jet parameters that are used for the jet models in this paper [9]. Some properties of under-dense jets will be treated in the section 2.6.

2.6 Jet-head advance speed

The velocity with which a jet penetrates into the ambient medium is less than the bulk velocity of jet material. This is especially true for under-dense jets. Near the point where the jet impacts with the ambient intergalactic/interstellar medium, a structure forms including a forward bow shock that precedes the jet, a contact discontinuity separating shocked ambient gas from shocked jet material and a reverse shock (Mach disk) that decelerates the jet flow. This whole system comprises the *jet-head*.

The jet-head advance speed can actually be estimated from ram pressure arguments in the rest frame of the head, where the flow is more-or-less steady (Marti et al. 1997; Rosen et al. 1999). The jet-head advance speed found in this way equals:

$$\beta_{\rm hd} = \frac{\gamma_{\rm jt}\sqrt{\eta_{\rm R}}\,\beta_{\rm jt}}{1+\gamma_{\rm jt}\sqrt{\eta_{\rm R}}}\ , \tag{30}$$

where again $\eta_{\rm R} = \rho_{\rm jt}/\rho_{\rm am}$ is the ratio of mass density of jet material and mass density of ambient medium material. In the case where the gas is relativistically hot, so that $h > 1$, the same expression holds, but then the ratio of mass densities is substituted by the ratio of relativistic enthalpies $\eta_{\rm R} \longrightarrow \rho_{\rm jt}h_{\rm jt}/\rho_{\rm am}h_{\rm am}$.

From equation (30) it is immediately clear that under-dense jets with $\eta_{\rm R} << 1$ have propagation speeds much less than their bulk velocities, unless they are very relativistic with $\gamma_{\rm jt} >> 1$. Using the same parameters as we did in section 2.5 (resulting in a density ratio of $\eta_{\rm R} \sim 10^{-3}$ and a Lorentz factor of $\gamma_{\rm jt} \sim 3$ with corresponding $\beta_{\rm jt} = 0.943$), we find that the jet-head propagation speed is approximately $\beta_{\rm hd} \sim 8 \times 10^{-2}$. The jet-head advance speed, together with the length of the jet, yields an estimate for the time that the central engine has been active. We will use this method for analytically predicting the jet-head advance speed to compare with our simulations in section 4.

2.7 Jet properties: Rotation

2.7.1 *Jet angular momentum*

In steady, axisymmetric hydrodynamic flows the specific angular momentum $\lambda \equiv \gamma h R V_\phi$ (neglecting general-relativistic corrections) is conserved. Its value is set by the rotation of the wind source. Then, the azimuthal four-velocity decays as

$$\gamma h V_\phi = \frac{\lambda}{R}\ . \tag{31}$$

In axisymmetric and ideal MHD flows with a magnetic field $\boldsymbol{B} = \boldsymbol{B}_{\rm p} + B_\phi\,\hat{\boldsymbol{e}}_\phi$, the situation is different. There, the angular velocity Ω of poloidal field/flow lines, formally defined by

$$\Omega = \frac{V_\phi}{R} - \kappa\frac{B_\phi}{R}\ , \tag{32}$$

is constant along flow lines. Its value is set by conditions at the source of the wind. Here, $\kappa \equiv V_{\rm p}/B_{\rm p}$ is the ratio of the poloidal velocity and magnetic field, again a constant along flow lines.

Such axisymmetric MHD winds behave roughly as follows: close to the source, where the wind is sub-Alvénic in the sense that $\gamma V_{\rm p} \ll \left(B_{\rm p}/\sqrt{4\pi\rho_0 h}\right)\left(1-\Omega^2R^2/c^2\right)$ with $\rho_0 = \rho/\gamma$ the proper density, the wind rotates almost rigidly with

$$V_\phi \sim \Omega R\ . \tag{33}$$

This solid rotation is enforced by strong magnetic torques on the wind material. Although one can define a conserved specific angular momentum λ that has a mechanical, as well as a magnetic contribution, the *mechanical* angular momentum is obviously not conserved!

Well beyond the so-called Alfvén point, the point on a flow line where $\gamma V_{\rm p} = \left(B_{\rm p}/\sqrt{4\pi\rho_0 h}\right)\left(1-\Omega^2R^2/c^2\right)$, the flow speed is super-Alfvénic and magnetic torques become dynamically unimportant. There, the wind satisfies (31), but with the value of λ now set by Ω and the radius $R_{\rm A}$ of the Alfvén point:

$$\lambda = \mu\Omega\,R_{\rm A}^2\ , \tag{34}$$

where $\mu \equiv \mathcal{E}/c^2 \geqslant 1$ with $\mathcal{E}$ the conserved total energy per unit mass in the wind. This means that the value of λ can be much higher than in the hydrodynamic case, leading to a larger rotation speed far from the source.

2.7.2 *Continuous rotation profile*

Valid solutions of the radial force balance equation (8) allow for different values of the constants $V_{\phi,\rm sp}$ and $V_{\phi,\rm sh}$. Giving these constants a different value will result in a discontinuous rotation profile, where the most realistic scenario is the one where $V_{\phi,\rm sp} > V_{\phi,\rm sh}$. Close to the central engine, where the different jet regions (spine and sheath) are thought to be driven by different mechanisms, such a rotation profile seems a reasonable one. However, as the jet propagates through the ambient medium, mixing effects between jet spine and jet sheath are likely to wash out the discontinuity occurring at the jet spine-sheath interface. Therefore, the rotation profile at larger distances from the central engine is likely to be continuous. This leads us to choose the rotation constants equal to one maximum value: $V_{\phi,\rm sp} = V_{\phi,\rm sh} \equiv V_\phi$.

3 METHOD

3.1 The models, setup and initial conditions

In this paper, we simulate AGN jets with moderate Lorentz factors of $\gamma \sim$ a few, putting them into the trans-relativistic regime. We simulate a continuously driven homogeneous (H) jet and two structured spine-sheath jets (an isothermal (I) jet and a piecewise isochoric (A) jet) of which the radial profiles are treated in section 2.4.

All jets have constant and similar luminosity during their entire evolution. In a follow-up paper, we will be concerned with the case of two distinct episodes of jet activity for the same jet models

[8] At this distance, the jet is dominated by kinetic energy flux.

[9] It is worthwhile to note that the choice in parameter space is fairly large and that different choices for $L_{\rm jt}$, $T_{\rm am}$ or $\gamma_{\rm jt}$ could in principle result easily in different density ratios. However, it turns out that for most sets of realistic parameters, the density ratio will in general lie in the range of $\eta_{\rm R} \sim 10^{-3} - 1$, most of which correspond to under-dense jets. Our choice is therefore reasonable and corresponds to an under-dense jet at the lower end of the spectrum.

Table 1. Free parameters that were used for the jet inflow properties and the initialization of the ambient medium for the three jet models *H*, *I* and *A*.

Models	$L_{\rm jt}$ [10^{46} erg s^{-1}]		n [10^{-6} cm^{-3}]		γ		V_ϕ [10^{-3} c]		Γ		P [10^{-12} erg cm^{-3}]
	sp	sh	sp	sh	sp	sh	sp	sh	sp	sh	
H (homogeneous)	3.82		4.55		3.11		0.0		1		1.38
I (isothermal)	1.82	3.35	P/ρ = constant		6.0	3.0	1.0	1.0	5/3	5/3	according to eq. (13)
A (isochoric)	0.44	3.39	1.0	5.0	6.0	3.0	1.0	1.0	5/3	5/3	according to eq. (19)
External medium	-		1.0×10^3		-		-		5/3		1.38

Kinetic luminosity ($L_{\rm jt}$), number density (n), Lorentz factor (γ), azimuthal velocity (V_ϕ), polytropic index (Γ), gas pressure (P). In case of model *H*, the jet is homogeneous in the radial direction and is described by single-valued quantities. The pressure in the ambient medium follows from the number density $n_{\rm am}$ and assuming a temperature of the ambient medium of $T_{\rm am} = 10^7$ K. The parameters for models *I* and *A* are initialized separately for jet spine (denoted as "sp" in the table) and jet sheath (denoted as "sh" in the table). In case of the models *I* and *A*, the pressure varies radially, as indicated. In case of the *I* model, the density varies radially in order to keep the temperature constant.

H, *I* and *A*. In order to make a clear distinction between the two cases, we introduce an index '1' for the steady case and introduce an index '2' for the case of episodic activity. Therefore, this paper will treat the simulations *H*1, *I*1 and *A*1.

The simulations have been performed on the same spatial domain for a duration of ∼ 23 Myr (22.8 Myr) with a kinetic luminosity of $L_{\rm jt} \sim 4 - 5 \times 10^{46}$ erg s^{-1}. The jets are injected into a warm-hot intergalactic medium with constant density ($n_{\rm am} = 10^{-3}$ cm^{-3}) and constant temperature ($T_{\rm am} = 10^7$ K), which is a reasonable approximation for the conditions inside a cluster of galaxies, at large distances from the central engine. The time steps are dynamically determined by the code, but are on the order of 270 yr.

Our jets are cylindrically symmetric with their jet axis along the $Z-$axis. At the start of the simulation the jet protrudes along its axis into the computational domain over a distance equal to its initial radius, which we choose $R_{\rm jt} = 1$ kpc for all three models. In the case of structured jets, this is equivalent to the outer jet sheath radius. For these jets we choose (in absence of observational constraints, and in accordance with Meliani & Keppens 2009) the radius of the jet spine equal to $R_{\rm sp} = R_{\rm jt}/3$.

We choose the maximum rotation of the structured jets to be $V_\phi \sim 1 \times 10^{-3}$ [10].

The jets start out in pressure equilibrium with their surrounding, as described in section 2.4. After initialization, the jet flow is created by letting material flow into the computational domain through the boundary cells at the $Z = 0$ axis, between $R = 0$ and $R = R_{\rm jt}$. Except for the cells involved in injecting the jet material, all other cells in the lower boundary are free *outflow* boundaries. In addition, the *inflow* velocity of these cells is reduced to 20% of their original value, in order to avoid spurious numerical effects next to the jet inlet.

The size of our computational domain is (250×500) kpc^2. We choose a basic resolution of (120×240) grid cells and allow for four additional refinement levels. This results in an effective resolution of (1920×3840) grid cells. Therefore, we can resolve details up to (65×65) pc^2.

Table 1 gives an overview of the free parameters that were used for these simulations. Moreover, table 2 shows a list of characteristic variables that are used throughout the paper, and which apply to the plots.

[10] This is a fairly conservative choice compared to the value of the critical rotation for the isochoric jet, see section 5.4.2. Moreover, note that even though we simulate purely hydrodynamical jets at kpc scales, we assume they have all started out as fully magnetohydrodynamical jets.

Table 2. List of characteristic quantities shown in cgs units. These characteristic quantities apply throughout the paper.

Char. quantities	**symbol**	**cgs units**
Number density	$n_{\rm ch}$	10^{-3} cm^{-3}
Pressure	$P_{\rm ch}$	1.50×10^{-6} erg cm^{-3}
Temperature	$T_{\rm ch}$	1.09×10^{13} K

3.2 MPI-AMRVAC and numerical schemes

Our simulations employ the code MPI-AMRVAC (Keppens et al. 2012). It is a versatile code that allows for various discretization schemes, involving the use of different limiters in the reconstructions from cell centre to cell edge. It allows for adaptive mesh refinement and can be run parallel on multiple processors.

The simulations are performed with a special relativistic hydrodynamical module. We choose a 4-step 'Runge-Kutta' time-discretization scheme, in combination with a second order spatial Total Variation Diminishing Lax-Friedrichs scheme with a Koren limiter. This combination captures shocks well without exhausting computational resources.

MPI-AMRVAC can be initialized using conservative variables, which are advected as according to their fluxes calculated through (1). However, the variables can also be initialized as *primitive* variables, which MPI-AMRVAC then converts back to conservative variables. We choose to do the latter. In that case, the free parameters of the models are the mass-density ρ, the velocity $\boldsymbol{v}$ and the pressure P. Finally, MPI-AMRVAC needs to be initiated with a maximum value for the polytropic index Γ. We initialized the polytropic index as $\Gamma = 5/3$. This choice for Γ is consistent with the Mathews approximation (equations (5), (6) and (7)) for these parameters.

3.3 Tracers of jet material

In jets with radial structure, or in cases where jet activity is episodic, it is important to keep track of the various constituents (for example, jet, jet spine, jet sheath, or ambient medium). To that end we employ *tracers*, $\theta_{\rm A}(t, \boldsymbol{r})$, [11] that are passively advected by the flow from cell to cell. Appendix A treats the definition of the tracers employed here. The number of tracers that were used for each simulation varies from case to case. Basically, every constituent we would like to trace is initialized to $\theta = \theta_{\rm max} = +1$ in the

[11] The index *A* refers to a certain constituent *A* in the simulation.

region where this constituent is injected into the system. We put its value equal to $\theta = \theta_{\rm min} = -1$ elsewhere. For completeness sake, we will list the exact values for each simulation below.

H1: For the homogeneous steady jet we use one tracer, θ. We initialize this tracer to $\theta = +1$ for jet material, and $\theta = -1$ for the ambient medium.

A1 and *I1*: For steady jets with structure, we employ two tracers; $\theta^{\rm sp}$ for material from the jet spine and $\theta^{\rm sh}$ for material from the jet sheath. The tracer $\theta^{\rm sp}$ is initialized as $\theta^{\rm sp} = +1$ for material in the jet spine and $\theta^{\rm sp} = -1$ elsewhere. Equivalently, tracer $\theta^{\rm sh}$ was initialized as $\theta^{\rm sh} = +1$ for material in the jet sheath and $\theta^{\rm sh} = -1$ elsewhere.

Despite the fact that the tracers are initiated with values $\theta_{\rm A}(t, \boldsymbol{r}) = \pm 1$, as soon as they are advected, actual mixing as well as effects from numerical discretization will yield tracer values within a volume element $\delta V(t, \boldsymbol{r})$ between $-1 \leqslant \theta_{\rm A}(t, \boldsymbol{r}) \leqslant +1$. We will interpret the tracer value $\theta_{\rm A}(t, \boldsymbol{r})$ to directly correspond to the amount of constituent A in that volume element.

3.4 Mixing effects for various constituents

Based on the amount of various constituents in a given volume element $\delta V(t, \boldsymbol{r})$, we are able to study the amount of mixing between different constituents. The following sections give a detailed description of how mixing can be quantified.

The first type of mixing is called *absolute mixing* (Δ) and deals with the exact mass fractions of those constituents in a volume element. In that case $\Delta = 0$ means that the constituents have not mixed at all, while $\Delta = 1$ means that the mass fractions of the constituents in a volume element are equal, regardless of what those mass fractions are.

The second type of mixing is called *mass-weighted mixing* (Λ). For this type of mixing, the mass fraction of a constituent in a volume element is divided by the *total mass* of that constituent in the computational domain. It is therefore a measure of homogeneity: $\Lambda = 0$ means no mixing, while $\Lambda = 1$ means a completely homogeneous mixture.

3.4.1 *Mass fractions of multiple constituents in a volume*

When considering fluid volume elements, all material within one element $\delta V(t, \boldsymbol{r})$ (one grid cell) is the sum of all its constituents. While some models treat the contents of a volume element with a multiple fluid approach (i.e. different constituents having a different temperature, density, velocity, etc.), our numerical method averages these quantities out, so that each grid cell can be characterized by one mass density, one pressure, one velocity vector, etc., known as the *one-fluid approximation*. In that case, the total mass density $\rho(t, \boldsymbol{r})$ within $\delta V(t, \boldsymbol{r})$ is the sum of mass densities of the different constituents $\rho_k(t, \boldsymbol{r})$. For a system with N constituents, this can be written as:

$$\rho(t, \boldsymbol{r}) = \sum_{k=1}^{N} \rho_k(t, \boldsymbol{r}) = \rho(t, \boldsymbol{r}) \sum_{k=1}^{N} \delta_k(t, \boldsymbol{r}) \,, \tag{35}$$

where $\delta_k(t, \boldsymbol{r})$ is the mass fraction of constituent k within $\delta V(t, \boldsymbol{r})$, so that:

$$\sum_{k=1}^{N} \delta_k(t, \boldsymbol{r}) = 1 \,. \tag{36}$$

We are interested in the effect of mixing of two certain constituents A and B (e.g. jet spine material and jet sheath material, or jet material and ambient medium material). In that case we can write the sum of the mass fractions of the constituents as:

$$\sum_{k=1}^{N} \delta_k(t, \boldsymbol{r}) = \delta_{\rm A}(t, \boldsymbol{r}) + \delta_{\rm B}(t, \boldsymbol{r}) + \delta_{\Sigma}(t, \boldsymbol{r}) = 1 \,, \tag{37}$$

where $\delta_{\Sigma}(t, \boldsymbol{r})$ is the sum of all other components within $\delta V(t, \boldsymbol{r})$ [12]. In the simple case where the system only consists of two constituents (e.g. jet and ambient medium), one has $\delta_{\Sigma}(t, \boldsymbol{r}) = 0$. Since this derivation applies to all individual grid cells, we will drop the index $(t, \boldsymbol{r})$ from now on.

3.4.2 *Quantifying the amount of* **absolute** *mixing* Δ

To study the amount of mixing between the two constituents A and B, it is useful to define an *absolute mixing factor* $\Delta_{\rm AB}$, which considers the absolute amount of the mass fractions within that cell. We choose $\Delta_{\rm AB} = 0$ in the case of no mixing by which we mean that only one of the two components A or B is present within δV and therefore $\delta_{\rm A} = 0$ *or* $\delta_{\rm B} = 0$. We choose $\Delta_{\rm AB} = 1$ in the case of maximum absolute mixing by which we mean the same amount of constituents A and B are present within δV, so $\delta_{\rm A} = \delta_{\rm B}$. Furthermore, we impose a linear scaling between the mass fractions within the cell and the amount of absolute mixing. These assumptions completely determine the definition of the absolute mixing factor for two different constituents in a cell: [13]

$$\Delta_{\rm AB} \equiv 1 - \left| \frac{\delta_{\rm A} - \delta_{\rm B}}{\delta_{\rm A} + \delta_{\rm B}} \right| \,. \tag{38}$$

In theory, one can also consider the more general case of mixing between two *sets* of constituents; one with a total mass fraction δ_{Σ_1} and a second with a total mass fraction δ_{Σ_2}. In that case formula (38) still applies, however, the indices A and B will then replaced by the indices Σ_1 and Σ_2. In this paper, we will only be concerned with the mixing of individual constituents.

3.4.3 *Quantifying the amount of* **mass-weighted** *mixing* Λ

Absolute mixing is a useful concept for situations where one is interested in the exact amounts of the constituents within that volume. It will, however, not always give an intuitive sense for the amount of homogeneity of the mixture.

To illustrate this, consider a fixed volume V which is made up of two constituents A and B, with total masses $M_{\rm A}$ and $M_{\rm B}$, and their sum $M = M_{\rm A} + M_{\rm B}$. At first, these two constituents are unmixed and separated by a wall, dividing V into equal two parts $\frac{1}{2}V$. We then remove the wall and stir up the constituents. When the

[12] Note that this can either simply be *the ambient medium*, but it could in theory also be a whole collection of other constituents.

[13] One subtle point must be made regarding this definition of the absolute mixing factor. If a volume element δV would contain neither of constituent A or B (and therefore $\delta_{\rm A} = \delta_{\rm B} = 0$), the absolute mixing factor is not clearly defined since the second term would yield a value 0/0.

In this particular case, we define the absolute mixing factor $\Delta_{\rm AB}$ as first taking one of the two mass fractions equal to 0 (so say $\delta_{\rm A} = 0$) and then formally taking the other mass fraction equal to 0 (so say $\delta_{\rm B} = 0$). After having taken the first mass fraction equal to 0, one is left with $1 - \left|\pm\frac{\delta_{\rm B}}{\delta_{\rm B}}\right|$, which always yields a value of 0, regardless of the value of the mass fraction $\delta_{\rm B}$. Therefore, the absolute mixing in the case of absence of both constituents is per definition equal to $\Delta_{\rm AB} = 0$.

constituents have had the time to settle down and maximally mix with each other, the resulting mixture is homogeneous with mass density $\rho = \frac{M}{V}$. The two mass fractions in every single cell in this case are $\delta_A = \frac{M_A}{M}$ and $\delta_B = \frac{M_B}{M}$. If M_A and M_B were not equal to begin with, even though the mixture is completely homogeneous, the absolute mixing will be unequal to one:

$$\Delta_{AB} = 1 - \left|\frac{M_A - M_B}{M_A + M_B}\right| \neq 1. \tag{39}$$

It is possible to introduce another quantity which will yield a value of one for homogeneous mixtures. To this end, we define the *mass-weighted mixing factor* Λ_{AB} in the same way as the absolute mixing factor, but now the mass fractions δ_A and δ_B are weighted by their *total mass* M_A and M_B contained in the total volume V:

$$\Lambda_{AB} \equiv 1 - \left|\frac{\delta_A - \mu_{AB}\delta_B}{\delta_A + \mu_{AB}\delta_B}\right| , \tag{40}$$

with $\mu_{AB} = \frac{M_A}{M_B}$ the mass ratio of constituent A and B. If we start out with unequal amounts of mass M_A and M_B, the mass-weighted mixing factor will yield a value of $\Lambda_{AB} = 1$ when the mixture has reached a homogeneous state. In that case the intuitive meaning of *mixed well* simply means $\Lambda \longrightarrow 1$.

3.5 Absolute mixing and mass-weighted mixing from tracer values

In the previous sections we calculated the amount of absolute mixing and mass-weighted mixing, based on the mass fractions δ_A and δ_B within a volume element δV. In this section, we express the amount of absolute and mass-weighted mixing in terms of the tracer values θ_A and θ_B in each grid cell. In this way, we are able to find the amount of absolute and mass-weighted mixing between different constituents in the jet simulations.

3.5.1 Absolute mixing from tracer values

As a tracer $\theta_A(t, \boldsymbol{r})$ is advected by the flow, it obtains values within the range $\theta_{min} \leqslant \theta_A(t, \boldsymbol{r}) \leqslant \theta_{max}$. Here θ_{min} corresponds to the absence of constituent A within this cell, whereas θ_{max} corresponds to a cell purely containing the constituent A. Since we interpret a tracer value to correspond directly to the amount of that constituent in a linear way, the mass fraction of A within grid cell $\delta V(t, \boldsymbol{r})$ is expressed by:

$$\delta_A(t, \boldsymbol{r}) = \left|\frac{\theta_A(t, \boldsymbol{r}) - \theta_{min}}{\theta_{max} - \theta_{min}}\right|. \tag{41}$$

With our choice of $\theta_{min} = -1$ and $\theta_{max} = +1$, the mass fraction of constituent A equals (dropping the index $(t, \boldsymbol{r})$ again):

$$\delta_A = \frac{1}{2}\,|\theta_A + 1|\ . \tag{42}$$

The mass fraction δ_B for constituent B is found by changing the label $A \longrightarrow B$. Therefore, the absolute mixing factor between constituents A and B in terms of their tracer values in grid cell δV can be written as:

$$\Delta_{AB} = 1 - \left|\frac{|\theta_A + 1| - |\theta_B + 1|}{|\theta_A + 1| + |\theta_B + 1|}\right| . \tag{43}$$

3.5.2 Absolute mixing between jet and shocked ambient medium

In case of the homogeneous jet $H1$, there is just one jet constituent present and so we have one tracer θ. From equations (36) and (42), we find that the mass fraction of the (shocked) ambient medium in terms of the jet tracer value θ in this case equals:

$$\delta_{am} = 1 - \delta_\theta = 1 - \frac{1}{2}\,|\theta + 1|\,. \tag{44}$$

Substituting these values into the absolute mixing factor (38) leads to the absolute mixing Δ between jet material and shocked ambient medium for the homogeneous jet:

$$\Delta = 1 - \big||\theta + 1| - 1\big|. \tag{45}$$

3.5.3 Mass-weighted mixing from tracer values

When dealing with two different jet constituents, the mass-weighted mixing factor in terms of tracer values translates to:

$$\Lambda_{AB} = 1 - \left|\frac{|\theta_A + 1| - \mu_{AB}|\theta_B + 1|}{|\theta_A + 1| + \mu_{AB}|\theta_B + 1|}\right| . \tag{46}$$

Using the same reasoning as before, the mass-weighted mixing factor between a homogeneous jet and the shocked ambient medium can be written as:

$$\Lambda = 1 - \left|\frac{(1 + \mu_{jt-am})|\theta + 1| - 2\mu_{jt-am}}{(1 - \mu_{jt-am})|\theta + 1| + 2\mu_{jt-am}}\right| , \tag{47}$$

with $\mu_{jt-am} = \frac{M_{jt}}{M_{am}}$. Here, M_{jt} is the total mass that is injected by the jet into the cocoon and M_{am} is the mass of the shocked ambient medium contained in the cocoon at time t. The approximations of M_{jt} and M_{am} will be calculated in the next two sections.

3.5.4 Total mass-energy discharge of the jet

The total mass M_{jt} is equal to the energy-mass discharge through the Mach disk, integrated over time t [14]. Using the rules for velocity addition in special relativity, it can be shown that the energy-mass discharge through the Mach disk for a steady homogeneous jet is:

$$M_{jt} = A_{jt}\rho_{jt}\gamma_{jt}\gamma_{hd}\left(v_{jt} - v_{hd}\right)t\ , \tag{48}$$

with A_{jt} the surface of discharge which we take equal to $A_{jt} = \pi R_{jt}^2$ and as before, ρ_{jt} the proper mass density, γ_{jt} and γ_{hd} the Lorentz factors of bulk jet material and jet-head, respectively (measured in the observer's frame) and equivalently for the velocities v_{jt} and v_{hd}.

We consider very under-dense jets where the jet-head propagation speed is small compared to the bulk velocity ($v_{hd} \ll v_{jt}$). In that case, the total mass injected by the jet into the cocoon is approximated by:

$$M_{jt} \approx A_{jt}\rho_{jt}\gamma_{jt}v_{jt}t\ . \tag{49}$$

The total energy-mass discharge for jet spine and jet sheath are calculated in similar fashion. In that case the indices "jt" are replaced by either "sp" for the jet spine, or "sh" for the jet sheath, and the correct corresponding surface areas need to be considered. With these expressions for the total masses M_{sp} and M_{sh}, we find a mass ratio between jet spine and jet sheath material equal to:

$$\mu_{sp-sh} = \frac{M_{sp}}{M_{sh}} = \frac{\rho_{sp}\gamma_{sp}v_{sp}}{(A_{jt}/A_{sp} - 1)\rho_{sh}\gamma_{sh}v_{sh}} = \frac{\rho_{sp}v_{sp}}{4\rho_{sh}v_{sh}}\ . \tag{50}$$

[14] We assume the energy-mass discharge through the Mach disk to remain constant during the entire simulation. Therefore, we will use the initial conditions at the jet inlet in order to calculate the energy-mass discharge of the jet.

Substituting the exact values for the isochoric jet results in $\mu_{\rm sp-sh} = 0.052$. In case of the isothermal jet, we interpolate for the average mass density in the jet spine and the jet sheath to find $\mu_{\rm sp-sh} = 0.217$.

3.5.5 *Total mass of the shocked ambient medium*

Finally, we approximate the total mass of the shocked ambient medium $M_{\rm am}$ by the volume containing this shocked material $V_{\rm co}^{\rm am}$, multiplied by the average local mass density in this volume $\rho_{\rm co}^{\rm am}$. For $V_{\rm co}^{\rm am}$ we take the volume of the cocoon $V_{\rm co}$ minus the volume bounded by the contact discontinuity $V_{\rm cd}$:

$$V_{\rm co}^{\rm am} = V_{\rm co} - V_{\rm cd} \approx \frac{3}{4} V_{\rm co} \ , \tag{51}$$

where we have approximated $V_{\rm cd} \approx \frac{1}{4} V_{\rm co}$ [15]. This material is actually *shocked* ambient medium, where the density is approximately compressed by a factor of $r \approx 4$. This yields:

$$M_{\rm am} = \rho_{\rm co}^{\rm am} V_{\rm co}^{\rm am} \approx 3 \rho_{\rm am} V_{\rm co} \ . \tag{52}$$

With these expressions for the total masses $M_{\rm jt}$ and $M_{\rm am}$, we find a mass ratio between shocked jet and shocked ambient medium material equal to:

$$\mu_{\rm jt-am} = \frac{M_{\rm jt}}{M_{\rm am}} \approx \frac{A_{\rm jt} \rho_{\rm jt} \gamma_{\rm jt} v_{\rm jt} t}{3 \rho_{\rm am} V_{\rm co}} \ . \tag{53}$$

Taking the values from the simulation of the homogeneous jet, as they occur after 23 Myr, we find a mass fraction ratio of $\mu_{\rm jt-am} \approx 3.06 \times 10^{-6}$. The mass ratios $\mu_{\rm jt-am}$ for the homogeneous jet and $\mu_{\rm sp-sh}$ for the isothermal jet and for the isochoric jet will be used extensively in the section 4 to determine the level of homogeneity of mixing between different constituents.

3.6 The relation between the effective polytropic index $\Gamma_{\rm eff}$ and the temperature T

In equation (5) we've already seen the effective polytropic index $\Gamma_{\rm eff}$ that describes a realistic transition between a non-relativistic gas and a relativistic gas, based on the particle rest-mass energy $m_{\rm p}c^2$ (re-introducing c for the moment) and the average thermal energy per particle $\epsilon_{\rm th}$. When this energy $\epsilon_{\rm th}$ becomes comparable to the rest-mass energy of the particle, the gas becomes relativistic. We therefore define the transition from non-relativistic to relativistic at the point where $k_{\rm b}T = m_{\rm p}c^2$. This implies that the gas becomes relativistic when the effective polytropic index drops below $\Gamma_{\rm eff} = 1.417$ (which comes from putting $\epsilon_{\rm th} = m_{\rm p}c^2$ in equation (5)). Since there is a one-to-one correspondence between $\Gamma_{\rm eff}$ and the temperature T, this also introduces a thermal temperature at which the proton gas becomes relativistic, namely $T_{\rm ch} \equiv \frac{m_{\rm p}c^2}{k_{\rm b}} = 1.09 \times 10^{13}$ K.

Figure 2 shows a cut along the jet axis of the steady homogeneous jet after 22.8 Myr. At this time, several internal shocks have developed, heating the jet material. Up to the point where the temperature is approximately 10^{12} K, the (proton) gas can still be described as non-relativistic. Only near the Mach disk at $Z \sim 400$ kpc, the temperature approaches 10^{13} K and there indeed the effective polytropic index drops to relativistic values.

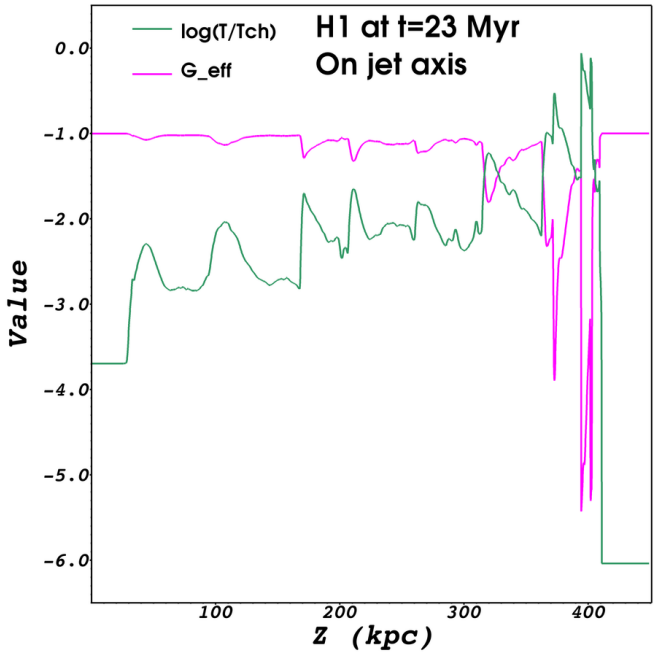

Figure 2. A cut along the jet axis of a homogeneous jet after 22.8 Myr. The plot shows the $\log_{10}$ of the thermal temperature T in units of the characteristic temperature $T_{\rm ch} = 1.09 \times 10^{13}$ K (green) and the rescaled effective polytropic index $G_{\rm eff}$ (pink) which represents a non-relativistic equation of state for $G_{\rm eff} = -1$ and a relativistic equation of state for $G_{\rm eff} = -6$ (occurring at $T \sim T_{\rm ch}$).

Note that we have actually plotted a quantity $G_{\rm eff}$ here, which is a rescaled version of the effective polytropic index:

$$G_{\rm eff} = 5 \left[3 \left(\Gamma_{\rm eff} - \frac{4}{3} \right) \right] - 6 \ , \tag{54}$$

in order to make the variations of the effective polytropic index more clear. The rescaled polytropic index has values that lie between $-6 \leqslant G_{\rm eff} \leqslant -1$, such that $G_{\rm eff} = -1$ corresponds to the classical equation of state $\Gamma = 5/3$ and $G_{\rm eff} = -6$ to a relativistic equation of state $\Gamma = 4/3$.

4 RESULTS

4.1 Jet-head advance speed from the simulations

In section 2.6, we showed that the jet-head advance speed can be estimated from ram-pressure arguments. There, we assumed both the Mach disk and the bow shock of the jet-head to be strong shocks. In addition, we assumed the pressure of the jet material behind the Mach disk and the ambient medium behind the bow shock to be equal. These are reasonable approximations for a homogeneous jet. However, in case of a jet with a fast moving jet spine and slower moving jet sheath, or when instabilities are taken into account, a simple (quasi-1D) analytical derivation will no longer be possible because of a complex flow structure near the head of the jet, see figures 6 (**A, B** and **C**).

[15] In the "ideal case" where there would be no instabilities causing turbulent mixing, the cocoon would consist of two regions separated by the contact discontinuity; the inner region $V_{\rm cd}$ containing purely shocked jet material and the outer region $V_{\rm co}^{\rm am}$ containing purely shocked ambient medium. In the realistic case where instabilities and turbulent mixing do occur, this outer region could in principle mix with shocked jet material. That is why we consider the volume $V_{\rm co}^{\rm am}$ for calculating the mass of the interacting ambient medium.

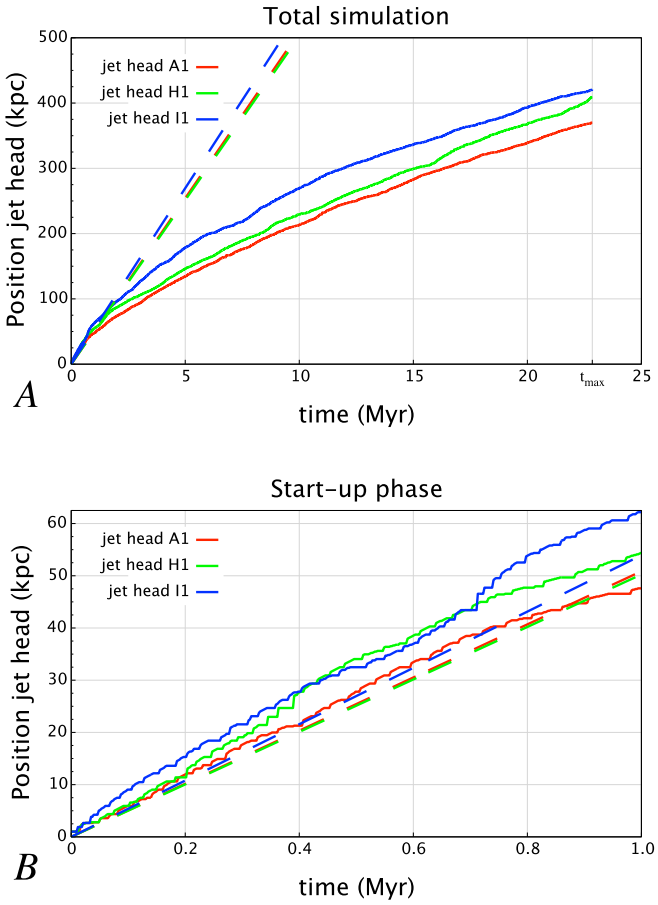

Figure 3. Jet-head propagation for all the steady jets $H1$, $I1$ and $A1$. The solid lines show the results from the simulations, the dashed lines show the analytically predicted values. Figure **A** shows the full duration of the simulation (up to t_{max} = 22.8 Myr). The jet-head propagation is not constant, but decelerates after a start-up phase of ∼ 1 Myr. The start-up phase of the simulations can be seen in figure **B**.

Despite the numerous processes that can influence the velocity of the jet-head, we would like to make a comparison between the simulations and the simple theory in section 2.6. In figure 3, we plotted the position of the jet-head as a function of time for all three different models. Plot 3 **A** shows the position of the jet-head for the full evolution of the simulations and plot 3 **B** shows the start-up phase ($\leqslant$ 1.0 Myr). It can clearly be seen that for all three models the jet-head velocities during the start-up phase are higher than during the rest of the simulation. During this phase, relatively little turbulence and instabilities have occurred in the cocoons. As can be seen in 3 **B**, the jet-head propagation for all three models during the start-up phase compares quite well with the analytically predicted values.

The analytically predicted value for the jet-head advance speed for the homogeneous jet $H1$ can directly be calculated from equation (30) and the values listed in table 1. In case of the isochoric jet $A1$, we calculate the jet-head advance speed, based on the parameters for jet spine and jet sheath separately and then take the area-weighted average of these velocities over the cross section of the jet. In case of the isothermal jet $I1$, we first calculate the average density of the jet spine and the average density of the jet sheath separately [16]. Then we calculate the advance speed for jet spine and jet sheath separately and finally take the area-weighted average. The jet-head advance speed from these theoretical calculations, the actual advance speed of the start-up phase of the simulations; and the actual advance speed at the final 2.8 Myr of the simulations are shown in table 3. We will discuss the slow-down of the jet-head advance speed from start-up phase to final phase in section 5.3.

Table 3. Jet-head advance speed (JHAS), jet radius before jet-head (R_{hd}) and effective impact radius (R_{eff}) for the models $H1$, $I1$ and $A1$.

JHAS, R_{hd} and R_{ext}	**units**	**H1**	**I1**	**A1**
Analytical prediction	[c]	0.164	0.176	0.164
Start-up phase (1.0 Myr)	[c]	0.174	0.199	0.152
Final phase (2.8 Myr)	[c]	0.047	0.032	0.035
Jet radius, just before head R_{hd}	[kpc]	∼ 5	∼ 6	∼ 7
Eff. impact radius R_{eff}	[kpc]	4.02	6.27	5.46

The first row shows the analytically predicted value for the jet-head advance speed. The second row shows the average advance speed over the first 1 Myr, where relatively little turbulence and instabilities have formed. The third row shows the average advance speed over the final 2.8 Myr. The fourth row shows the jet radius, just before the jet-head. The bottom row shows the effective impact radius of the area of the ambient medium that effectively impacts the jet.

4.2 Internal shocks along the jet axis

In figures 4 and 7, the simulations for the three steady jet models $H1$, $I1$ and $A1$ are shown at the end of the simulation, corresponding to a time t_{max} = 22.8 Myr. Moreover, most variables that we show in our line plots are dimensionless, given in units of the characteristic variables. Therefore, we indicated their values on the vertical axis as "*Value*".

The top panel of figure 4 (line plots **A, B** and **C**) shows a cut along the jet axis R = 0 kpc of three quantities, namely: ($\log_{10}$ of) the gas pressure P; the number density n; and the thermal temperature T, in units of their characteristic quantities.

The lower panel of figure 4 (line plots **D, E** and **F**) show a cut along the jet axis of the tracer values and the absolute and mass-weighted mixing factors Δ and Λ.

Several internal shocks appear along the jet axes, as can be seen in line plot 2 and line plots 4 (**A, B** and **C**). These shocks can be recognized by their strong jumps in density, temperature and pressure. Vortices that emerge at the jet-head break off at a certain point, after which they travel down the cocoon, along the jet axis. As we will discuss in section 4.12, these vortices are responsible for the internal shocks occurring along the jet axis. Roughly nine shocks are found in all three models $H1$, $I1$ and $A1$ along the jet axes at the final time of simulation.

The first internal shock after the jet inlet occurs fairly quickly for the $H1$, $I1$, and $A1$ jets. This might be somewhat unexpected since the jets are set up in pressure equilibrium with their surroundings. However, as soon as the jets start to plow through the ambient medium, a (forward) bow shock and a reverse shock (the Mach disk) form. Shocked ambient medium that crosses the bow shock and jet material that crosses the Mach disk are shock-heated at the jet-head. The shocked gasses flow downstream, away from

[16] The isothermal jet has a density profile that depends on radius.

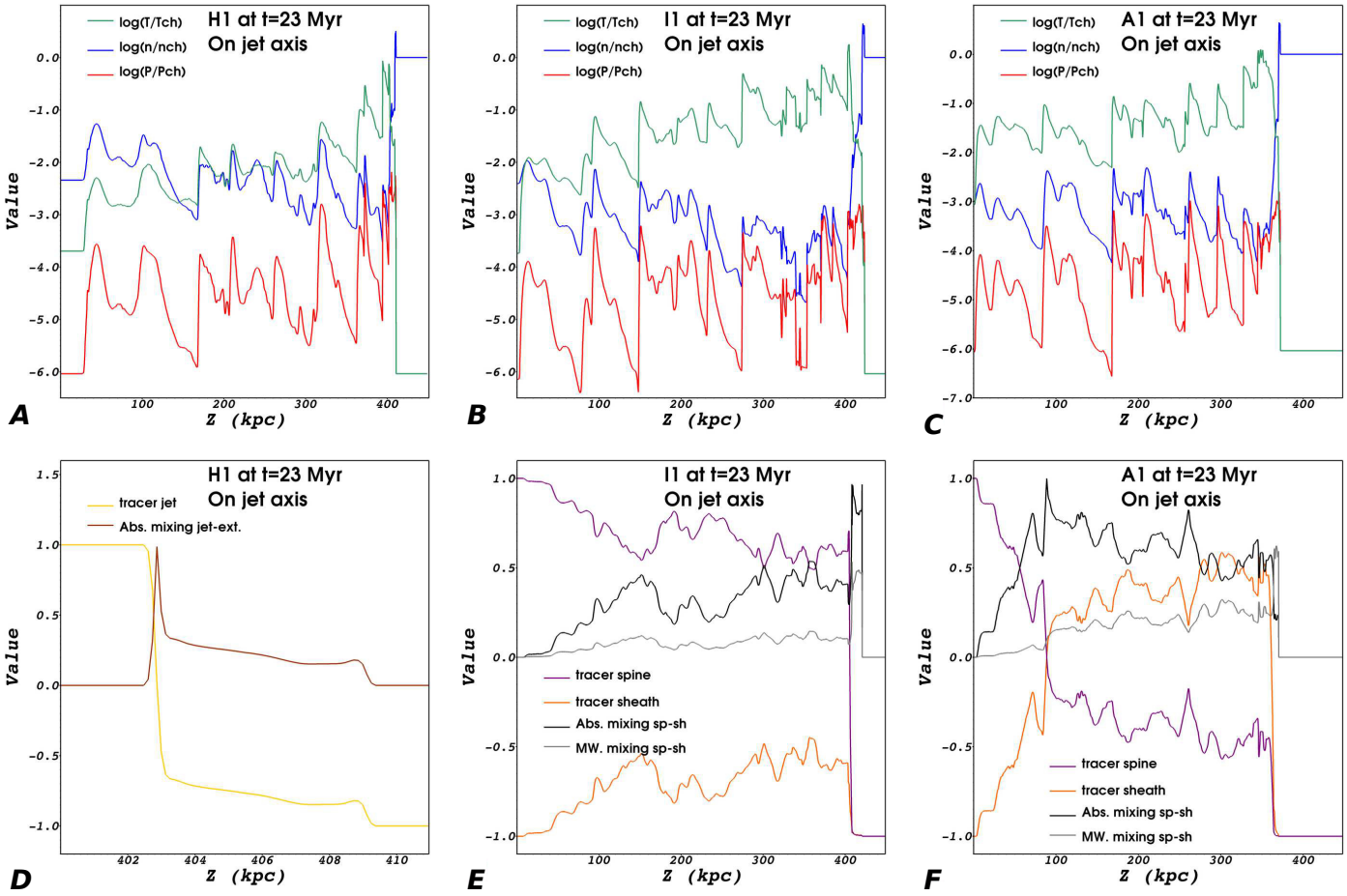

Figure 4. Cuts along the jet axis ($R = 0$ kpc) for the homogeneous jet $H1$ (left panels), the isothermal jet $I1$ (centre panels) and the isochoric jet $A1$ (right panels) at $t = 22.8$ Myr. Top panels **(plots A, B, C)** show the ($\log_{10}$ of) the number density in units of the characteristic number density $n_{\rm ch}$ (blue); the gas pressure in units of the characteristic pressure $P_{\rm ch} = 1.50 \times 10^{-6}$ erg cm^{-3} (red); and the thermal temperature T in units of the characteristic temperature $T_{\rm ch} = 1.09 \times 10^{13}$ K (green). The lower panel **(plots D, E, F)** shows tracer values and absolute and mass-weighted mixing. For the homogeneous jet (**plot D**), only the jet-head is shown, between $400 \leqslant Z \leqslant 410$ kpc. This is the only part along the jet axis where these variables show some variation. For the isothermal and isochoric jets (**plots E** and **F**), the tracer values of jet spine material $\theta^{\rm sp}$ (purple), the tracer of jet sheath material $\theta^{\rm sh}$ (orange), as well as the amount of internal absolute mixing (black) and the amount of internal mass-weighted mixing (gray) between jet spine and jet sheath material are shown.

the jet-head. This causes the pressure to rise to $P_{\rm co} \sim 10^2\ P_{\rm am}$ inside the cocoon. Since the pressure is kept constant at the jet inlet, the jet quickly becomes under-pressured compared to the cocoon. As a result, the jet is compressed and a structure containing a compression fan and a shock is formed. This shock tries to re-establish pressure equilibrium between the jet and the surrounding cocoon. These adjustment shocks are an artifact of the boundary conditions applied in the simulations and will not occur in actual jets. However, a new pressure equilibrium is formed fairly quickly after the jet inlet. Therefore, we expect the influence of the adjustment shock on the further evolution of the systems to be small.

The global behavior of the internal shocks for the three models are similar: After the adjustment shock, a second strong shock is located at $Z \sim 75 - 90$ kpc and a third strong shock occurs at $Z \sim 140 - 170$ kpc. After these three strong internal shocks more shocks follow. These shocks are less strong than the previous shocks, the separation between these shocks is smaller and they show more chaotic behavior, i.e. fluctuations in pressure, density and temperature along the jet axis. The final and strongest shock occurs at the jet-head. In this Mach disk, the jet material is shock-heated to relativistic temperatures.

The main differences between the individual models are as follows: For the $H1$ jet, the adjustment shock occurs at a slightly larger distance from the jet inlet ($Z \sim 30$ kpc) than for the $I1$ and $A1$ jets (both $Z \sim 5$ kpc). A second distinction that can be made is the form of the shocks. The $H1$ jet shows clear distinct shocks, where each shock is represented by a single peak in density, pressure and temperature. The $I1$ jet on the other hand has more variable behavior. Each shock is followed by a few small variations in the density, pressure and temperature. Finally, the $A1$ jet shows the most variable behavior: each individual strong shock is followed by a number of (typically 2) weaker shocks. Therefore, based on the internal structure of the jets along the jet axis, the $H1$ jet is the most regular jet, the $I1$ jet comes next and finally the $A1$ jet is the least regular jet.

4.3 Temperature along the jet axis

The temperature along the jet axis for the three different jet models shows some general behavior: it is strongly coupled to the occurrence of internal shocks. Each shock heats up the jet material. The rise in temperature leads to a strong increase in pressure, which

in turn causes the jet to expand sideways. This expansion leads to a decrease in temperature, but along the jet axis, the temperature shows an overall increase all the way up to the jet-head.

The behavior of the temperature for the individual models is as follows: The $H1$ jet at jet inlet ($Z = 0$ kpc) has a temperature of $T \sim 2.1 \times 10^9$ K. After the first (adjustment) shock at $Z \sim 30$ kpc, the temperature rises to $T \sim 5.5 \times 10^{10}$ K. Then finally after the Mach disk, the temperature rises up to $T \sim 9.7 \times 10^{12}$ K.

The temperature of the $I1$ jet also has a value of $T \sim 2.1 \times 10^9$ K at the jet inlet (as it is set up). However, already after the first shock the temperature increases to $T \sim 1.4 \times 10^{11}$ K. At the Mach disk the temperature rises up to $T \sim 1.4 \times 10^{13}$ K, putting it well into the relativistic regime and making it the hottest jet of the three models (as seen on the jet axis).

Finally, the temperature of the $A1$ jet at jet inlet is $T \sim 9.1 \times 10^9$ K (so higher than the other jets by a factor of ~ 4.5). At the first shock, the temperature rises to $T \sim 3.9 \times 10^{11}$ K. At the jet's head, the temperature reaches its highest value, $T \sim 1.1 \times 10^{13}$ K, again putting it into the relativistic regime.

4.4 Mixing effects along the jet axis

In this subsection we will discuss the amount of mixing *along the jet axis* (line plots 4 **D, E** and **F**). None of the three jets mix with shocked ambient medium from the cocoon at a notable level at any point along the jet axis. The simulations show that only a very small fraction of shocked ambient medium is entrained by the jet. In line plot 4 **D** for the $H1$ jet, this can directly been seen from the fact that the absolute mixing factor $\Delta \sim 0$, except at the jet-head. In case of the spine-sheath jets (line plots 4 **E** and **F**), this is seen from the fact that the sum of the jet spine and jet sheath tracers always add up to $\sim$ zero, so that each grid cell inside the jet, along the jet axis, contains little or no entrained material from the ambient medium. Therefore, the jets maintain their stability along the jet axis.

In case of the spine-sheath jets, however, the structural integrity of the jets is not necessarily maintained along the jet axis. Even though no mixing with the ambient medium occurs along the jet axis, jet spine and jet sheath material within the jets are capable of mixing due to effects such as the Kelvin-Helmholtz instability, strong internal shocks or the formation of vortices. The next two subsections will treat these mixing effects along the jet axis for the $I1$ jet and the $A1$ jet separately.

4.4.1 The isothermal jet $I1$

Line plot 4 **E** shows the mixing behavior between jet spine and jet sheath for the isothermal jet. At the jet inlet ($Z = 0$), the jet consists of pure jet spine material. This corresponds with the initialization of the jet ($\theta^{\rm sp} = +1$ and $\theta^{\rm sh} = -1$). Therefore, the absolute mixing factor, as well as the mass-weighted mixing factors are both zero ($\Delta_{\rm sp-sh} = \Lambda_{\rm sp-sh} = 0$).

As one moves towards the jet-head, the amount of mixing increases. However, the internal shocks that occur along the jet axis do not significantly correlate with the internal mixing between jet spine and jet sheath material. There is gradual increase in the amount of mixing up to $Z \sim 150$ kpc from the jet inlet, where the absolute mixing approaches a peak of $\Delta_{\rm sp-sh} \sim 0.5$. This peak is the only point that coincides with a strong shock at $Z \sim 150$ kpc. Moving further towards the jet-head, the absolute mixing varies slightly, but never exceeds $\Delta_{\rm sp-sh} = 0.5$. Then finally at the Mach disk, the absolute mixing becomes maximal and attains values of $\Delta_{\rm sp-sh} \longrightarrow 1$.

The mass-weighted mixing is small and never exceeds $\Lambda_{\rm sp-sh} \sim 0.1$. Therefore, despite the fact that there is some (internal) mixing between jet spine and jet sheath, the level of mixing is only $\sim 10\%$ compared to a fully homogeneous mixture.

The tracers don't intersect anywhere along the jet axis. The physical meaning of this is that the material on the jet axis consists almost entirely of jet spine material, all the way up to the jet-head. We therefore expect that, based on the amount of jet spine and jet sheath constituents, the spine-sheath jet structure can be recognized all the way to the jet-head.

4.4.2 The isochoric jet $A1$

As in the case of the isothermal jet, we see that the isochoric jet at inlet consists of pure jet spine material (line plot 4 **F**). There are two features which clearly differ from the isothermal case: First of all, we see a strong correlation between the location of the internal shocks and the increase in the level of (absolute-, as well as mass-weighted) mixing. Secondly, the tracer values $\theta^{\rm sp}$ and $\theta^{\rm sh}$ both quickly approach zero at the second strong shock ($Z \sim 82$ kpc). Therefore, at that location, the mass fractions of jet spine and jet sheath are equal in those grid cells. After this strong internal shock, the tracers $\theta^{\rm sp}$ and $\theta^{\rm sh}$ switch signs. This means that from that point, moving towards the jet-head, the jet axis is dominated by jet sheath material. Therefore, the jet spine and jet sheath have undergone strong internal mixing, where the absolute mixing factor attains values of $\Delta_{\rm sp-sh} \sim 0.5 - 1$.

The mass-weighted mixing, on the other hand, remains fairly low ($\Lambda_{\rm sp-sh} \leqslant 0.3$), reflecting the fact that even though there has been considerable mixing between jet spine and jet sheath material along the jet axis, the mixture is far from homogeneous. This suggests that some radial structure should still be recognizable, however, a distinction between a jet spine and a jet sheath will probably no longer be visible. Section 5.4 discusses the explanation for this difference in the amount of mixing in more detail.

4.5 Radial cuts across the jets

In this section we will investigate the radial structure of the different jets by looking at *radial cuts* at various heights. Figure 5 shows radial cuts of the three individual jet models $H1$ (top row), $I1$ (middle row) and $A1$ (bottom row) at three different heights, all at the final time of simulation $t = 22.8$ Myr.

The radial cuts cover the region $R \leqslant 10$ kpc. Since the jets have an initial radius of $R_{\rm jt} = 1$ kpc, these plots show the jet, as well as part of the surrounding cocoon.

The jet axis in figure 5 is located at $R = 0$ kpc (left side of the line plots). From the jet axis moving outwards, the jets are represented by jet material having a Lorentz factor $\gamma > 1$. The jet boundary occurs at the point where the Lorentz factor becomes $\gamma = 1$. Beyond the jet boundary lies part of the cocoon, containing a mixture of shocked jet (spine and sheath) and shocked ambient medium. The transition between pure jet and cocoon is formed by a layer where the jet mixes with the cocoon. With increasing mixing, we see the bulk Lorentz factor decreasing.

We have chosen to study the radial structure of the individual jets at three different heights, where we expect different characteristics in the radial direction.

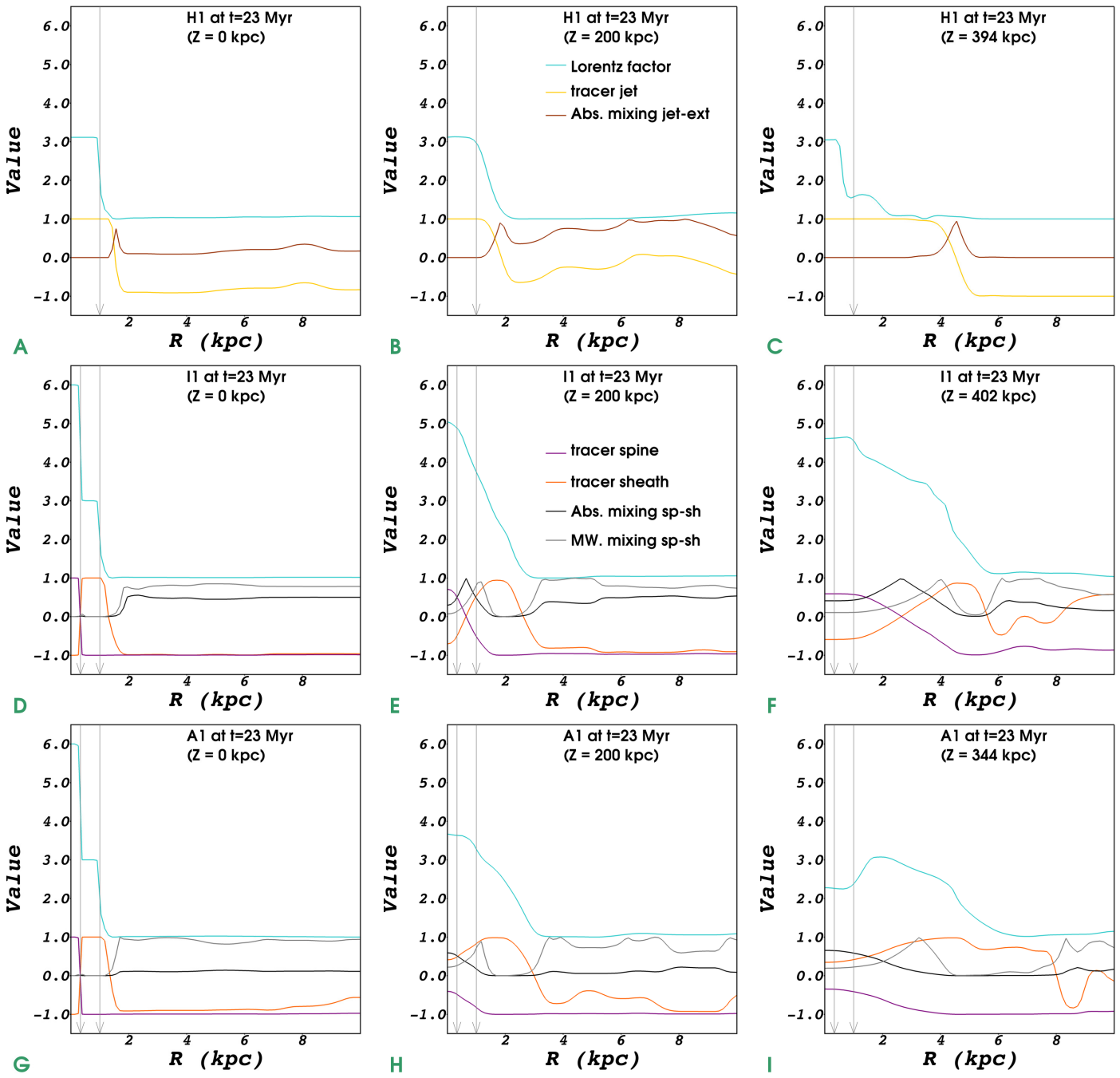

Figure 5. Radial cuts along the cylindrical radial direction at three different heights, showing Lorentz factor; tracer values; and the absolute- and mass-weighted mixing factor. The top row (**plots A**, **B** and **C**) shows radial cuts for model $H1$. The legend shown in figure **B** applies to the top row, except for the Lorentz factor which applies to all plots. The middle row (**plots D**, **E** and **F**) shows model $I1$. The legend shown in figure **E** applies to this middle row and the bottom row. The bottom row (**plots G**, **H** and **I**) shows model $A1$. In the first column, a radial cut is made at the jet inlet at $Z = 0$ kpc. In the second column a radial cut is shown at a distance $Z = 200$ kpc from jet inlet where all jets ($H1$, $I1$ and $A1$) have crossed three strong internal shocks. In the third column, a radial cut is shown just below the hot spot (where the effective polytropic index drops below $\Gamma_{\rm eff} \leqslant 1.417$). The exact location of the hot spot for these three jet models differs. The vertical arrows in all line plots (**A** through **I**) at $R = 1$ kpc mark the initial jet radius. The vertical arrows at $R \sim 0.3$ kpc mark the initial jet spine - jet sheath interface.

4.5.1 The jets at jet inlet

The left column (figures 5 **A**, **D** and **G**) shows a cut at the jet inlet at $Z = 0$ kpc, where the jets have just been injected into the domain. Here, the jets have only just had the chance to interact with the cocoon and have not passed any strong shocks. Therefore, the jets are still completely regular.

Figure 5 **A** shows the homogeneous jet. Up to its initial jet radius $R_{\rm jt} = 1$ kpc, it has Lorentz factor $\gamma_{\rm jt} = 3.11$ and consists of pure jet material $\theta = +1$. There is a sharp transition between jet and

cocoon at R_{jt}, where the absolute mixing with the cocoon quickly rises and falls off again.

Figures 5 **D** and **G** show the isothermal jet and the isochoric jet respectively. These jets have both been initiated with the same tracer values (pure jet spine material from jet axis up to $R_{sp} = R_{jt}/3$ and pure jet sheath material from R_{sp} up to R_{jt}) and Lorentz factors ($\gamma_{sp} = 6$ for the jet spine and $\gamma_{sh} = 3$ for the jet sheath) in radial direction. This is clearly seen in the plots. Moreover, within the jets, there is very little internal mixing between jet spine and jet sheath material.

4.5.2 The jets after three strong shocks

The centre column (5 **B**, **E** and **H**) shows a radial cut at $Z = 200$ kpc. We consider this height because we know (from the previous subsection, where we discussed the mixing behavior along the jet axis) that all three jets have passed three strong internal shocks at that height, and that the spine-sheath jets have had the chance to undergo strong internal mixing. This height is approximately half way from jet-inlet to jet-head.

Figure 5 **B** shows the homogeneous jet. We see that the jet has not significantly changed its structure compared to that at jet inlet. The jet is still completely intact up to its initial jet radius R_{jt}. The main difference is that the transition layer is now wider, so that the jet has effectively broadened to a radius of $\sim 2R_{jt}$.

In the isothermal jet (5 **E**) and the isochoric jet (5 **H**), considerable internal mixing between jet spine and jet sheath has occurred. The radial cut of the *I*1 jet shows that the inner part of the jet is still dominated by jet spine material. However, (as we also saw in the previous subsection) the inner part of the *A*1 jet is already dominated by jet sheath material. Therefore, the radial structure of the isothermal jet is less easily disrupted by internal shocks than that of the isochoric jet.

Looking at the radial cuts, moving from jet axis outwards to jet boundary, two forms of mixing occur. Already at the jet axis, jet spine and jet sheath mix internally. Both jets show a peak where the mass-weighted mixing becomes large ($\Lambda_{sp-sh} \sim 1$). This mixing results in a smooth radial profile of the Lorentz factor: The Lorentz factor at the jet axis has decreased compared to its initial value at jet inlet, resulting in $\gamma_{sh} < \gamma < \gamma_{sp}$. From the axis moving outwards, the Lorentz factor decreases with a decreasing amount of jet spine material, up to the point where only pure jet sheath material is present with $\gamma \sim \gamma_{sh}$. Moving out even further, the jet and the cocoon start to mix. This mixing further decreases the Lorentz factor, up to the jet boundary where $\gamma = 1$. Therefore, based on Lorentz factor alone, a spine-sheath jet structure will be hard to detect. However, looking at the abundance of jet spine and jet sheath material, a distinction can still be made. This distinction will be most prominent for the isothermal jet, where the jet core is still dominated by jet spine material, while the surrounding layer is dominated by jet sheath material.

At this height, the *I*1 jet has broadened to approximately $\sim 2.5R_{jt}$. The *A*1 jet, on the other hand has broadened to approximately $\sim 3R_{jt}$.

4.5.3 The jets just before the Mach disk

The right column (figures 5 **C**, **F** and **I**) shows cuts just before the jets cross the Mach disk, and therefore just before the hot spot. The height of this point varies between the individual models. We have chosen to look at the radial structure of the jet at this height, because we are interested in its behavior just before the jet is terminated at the final shock and because we want to know if a spine-sheath jet structure can survive all the way up to the jet-head.

Figure 5 **C** shows the radial cut of the homogeneous jet at a height of $Z = 394$ kpc. It is striking to see that even though the jet has passed ~ 9 shocks, the integrity of the core of the jet is still intact, with pure jet material and a Lorentz factor equal to its initial value. Moving outward in radial direction, the Lorentz factor decreases (less smoothly than at $Z = 200$ kpc), up to a radius of approximately $\sim 5R_{jt}$ which marks the jet boundary. The strongest mixing between jet and cocoon occurs in a transition layer between 4 and 5 kpc from the jet axis.

Figure 5 **F** shows a radial cut of the isothermal jet at a height of $Z = 402$ kpc. The radius of the jet has broadened to approximately $\sim 6R_{jt}$. It can be seen that the core of the jet is still dominated by jet spine material and the outer part still by jet sheath material. Within the jet, the jet spine and jet sheath have mixed slightly more than at $Z = 200$ kpc and the transition layers (the regions of strong internal jet mixing, as well as mixing between jet and ambient medium) have broadened. The internal mixing between jet spine and jet sheath, as well as the mixing between the jet and the cocoon are reflected in the radial profile of the Lorentz factor: The Lorentz factor decreases with increasing distance from the jet axis, but as with the homogeneous jet, the decrease occurs less smoothly than at $Z = 200$ kpc. The distinction between jet spine and jet sheath for the isothermal jet, based on Lorentz factor was already lost at $Z = 200$ kpc. This has not changed at the current height. However, based on the abundance of jet spine and jet sheath material, a clear distinction can still be made. In this regard we conclude that the isothermal spine-sheath jet structure survives all the way up to the jet-head.

Finally, figure 5 **I** shows the radial cut of the isochoric jet at $Z = 344$ kpc. The radius of the jet has broadened to approximately $\sim 7R_{jt}$, making it the widest jet of the three models, just before the hot spot. The jet spine and jet sheath material at the jet's centre have internally mixed slightly more than at $Z = 200$ kpc. The amount of jet spine material very gradually decreases with increasing distance from the jet axis up to $R \sim 4.5$ kpc, from which point on there is only pure jet sheath material present that immediately starts to mix with the surrounding cocoon. The Lorentz factor at this point even behaves rather counter-intuitively. Where one would expect a *higher* Lorentz factor at the jet's centre, the central part now has a *lower* Lorentz factor than the surrounding jet sheath. The reason for this becomes clear when we consider the jet flow at a distance slightly further from the jet-head. The simulation shows that there is a strong internal shock just before the hot spot at $Z \sim 340$ kpc. As mentioned before, a shock decelerates the jet flow, and only sufficiently far from the shock is the jet material able to re-accelerate due to pressure gradients when the jet re-establishes pressure equilibrium. In this case, the internal shock is so close to the hot spot, that the central part of the jet has not been able to fully re-accelerate. The outer part of the jet, however, is less strongly shocked by this internal shock. It is slightly deflected, and the Lorentz factor of the outer part of the jet is not significantly influenced, resulting in a higher value than its central part.

The spine-sheath jet structure becomes unrecognizable well before one reaches the hot spot: The jet spine and jet sheath material have almost completely mixed internally with each other. We conclude that the isochoric jet can not maintain its spine-sheath jet structure up to large distances from the central engine.

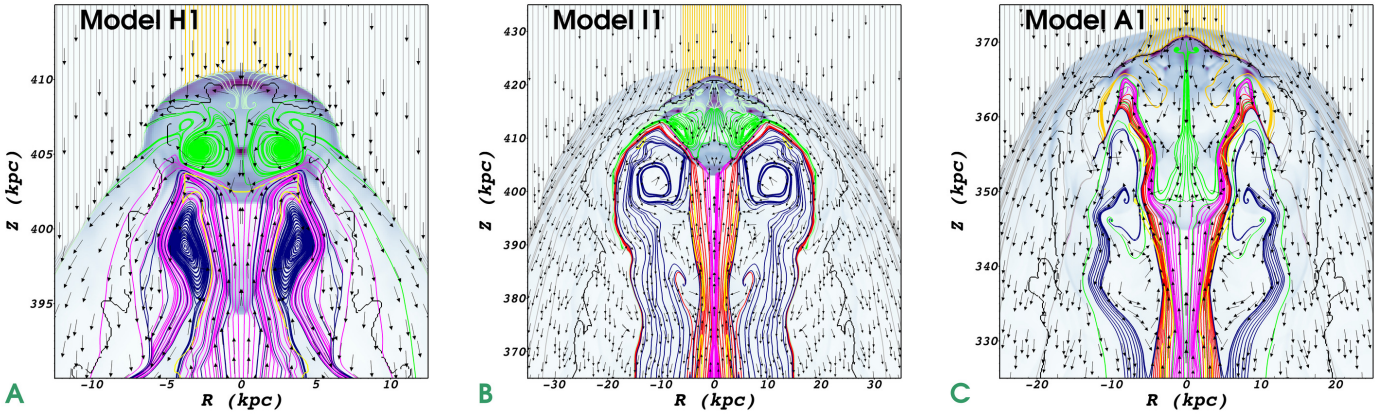

Figure 6. Close-up of the jet-head structure for the models $H1$, $I1$ and $A1$ at the final time of simulation, t = 22.8 Myr. Plot **A** shows the homogeneous jet, **B** the isothermal jet and **C** the isochoric jet. Various regions of the flow (in the frame of the advancing Mach disk) have been depicted by different flow line colors (see section 4.6 for a full explanation). The main features in the plots are: the jet flow; the effective impact area of the ambient medium that impacts the jet; and regions of vortex formation and turbulent mixing.

4.6 Flow properties in the jet-heads

In figures 6 (**A, B** and **C**), close-ups of the jet-heads are shown at the final time of simulation, t = 22.8 Myr. The blue color scale on the background represents the pressure, which clearly shows the bow shock of the jet-head and the Mach disk where the jet flow is terminated.

Velocity unit vectors are also drawn in the rest-frame of the advancing Mach disk. They show the direction of the undisturbed ambient medium flowing into the cocoon from the top of the plots, the direction of the inflowing jet material from the bottom of the plot and the direction of the flows within the cocoon itself. As expected, the velocity goes to zero at the Mach disk.

Flow lines (also as measured in the rest frame of the Mach disk) of various different regions marked with different colors are also shown.

Gray and *dark yellow* lines that start at the top mark the inflowing undisturbed ambient medium. Here, the dark yellow lines mark the effective impact area, the values of which are calculated in section 5.3).

Green flow lines (just below the bow shock) represent the shocked jet material and shocked ambient medium material. These flow lines show the exact behavior of the mixing of jet material and shocked ambient medium material at the top of the jet-head.

Pink and *red* flow lines (starting at the bottom centre) represent the jet flow. For the homogeneous jet $H1$ in figure 6 **A**, the entire jet flow is represented by pink lines. For the structured jets $I1$ and $A1$ in figures 6 **B** and 6 **C**, the red lines mark the part of the jet that contains the maximum mass fraction of jet sheath material across the cross section of the jet (which is on the order of $\sim 90\% - 100\%$). The pink lines mark the inner part on the jet flow where jet spine material is present. This region consists of a mixture of jet spine and jet sheath material.

Dark blue lines mark the region of back-flowing jet material that lies between the jet and the bulk of the back-flowing jet material. The morphology of these flow lines for the three models varies significantly from one model to the next, but in all three cases vortices are clearly seen.

Finally, two line contours are shown. The first contour is the black line within the bow shock. This contour encloses the region where jet material is found (which is derived from the presence of jet tracer material) [17]. The second is a yellow contour that resides within the jet flow. It marks the boundary of the jet flow, which we have taken to contain the largest mass fraction of jet material within the grid cells (which is $\sim 90\% - 100\%$).

We see that for the homogeneous jet $H1$ the pressure gradient at the top of the jet-head in plot 6 **A** is so large that the flow lines are strongly deflected outward along the bow shock. However, for the two jet-heads of the spine-sheath jets $I1$ and $A1$ in plots **B** and **C**, the pressure gradients at the bow shock are less strong, allowing the flow lines to penetrate the cocoon before they are deflected outwards. This can be explained by considering the Mach disk for the jet-heads of $H1$, $I1$ and $A1$. The Mach disk of the homogeneous jet $H1$ has a much larger surface area than the Mach disk of the structured jets $I1$ and $A1$. For the homogeneous jet, the entire jet flow is shocked by the Mach disk, but in case of the structured jets only the inner part of the jet flow is shocked by the Mach disk. This results in the fact that the pressure downstream of the Mach disk for the homogeneous jet becomes significantly higher than in case of the structured jets. The jet sheath material (the red flow lines) is able to propagate further into the jet-head structure than the jet spine material. When this jet sheath material then eventually encounter regions with high enough pressure, it is deflected and flows away from the jet-head, back into the cocoon.

By considering the bulk of back-flowing shocked jet material, we see that the black contour (enclosing the jet material) does not coincide very well with these (outermost) flow lines, but mostly lies outside this region. In the ideal scenario where no instabilities would develop at the jet-head, there would be a clear sudden transition between shocked jet material and shocked ambient medium material, separated by the contact discontinuity. In that case, the black contour would exactly correspond to the contact discontinuity. However, in the realistic case with instabilities, there will be a layer with a certain thickness instead of a contact discontinuity. The surface enclosing the bulk of back-flowing jet material corresponds to what we call the contact discontinuity. The layer surrounding

[17] The intermittency of the black contour is a result of the finite resolution of the simulations. Regardless, it still marks the boundary of the jet material containing region to good approximation.

that contact discontinuity can best be considered as shocked ambient medium material 'contaminated' with shocked jet material.

4.7 Large-scale behavior of jets and cocoons

In the next sections, we will focus on the behavior of material inside the cocoons. We will discuss properties such as cocoon shape, the distribution of densities and relativistic gas, mixing effects of shocked jet (spine and sheath) material and shocked ambient medium. Finally, we will link these large-scale cocoon properties to the properties that occur within the jets, the so-called effect of cocoon-jet coupling.

Figure 7 shows the contour plots of the jets and cocoons as they have developed after the full time of simulation $t = 22.8$ Myr. The top panel shows the distribution of number density ($n/n_{\rm ch}$) and relativistic gas ($\Gamma_{\rm eff}$), while the lower panel shows various forms of mixing. In all these contour plots, the $R-$axis has been stretched by a factor of 2.5 in order to enhance the visibility of the jets. The yellow contour marks the interface between the region consisting of purely shocked ambient medium and the region that contains a mixture of shocked jet material and shocked ambient medium. The green contour (mainly found at the jet-head) encloses relativistically hot regions ($\Gamma_{\rm eff} \leqslant 1.417$). A summary with the most notable characteristics of each individual model can be found in table 5.

4.8 Global morphology of the cocoons

After 22.8 Myr, the average distance traveled by the jets is $Z = 400$ kpc. Individual models differ from this mean value by a few tens of kpc. The isochoric jet $A1$ has traveled the shortest distance (370 kpc); the homogeneous jet $H1$ comes next (409 kpc); and the isothermal jet $I1$ has traveled the largest distance (421 kpc). The averaged maximum width of the cocoons is $R \sim 87$ kpc at an average distance of ~ 343 kpc from the jet-head.

All cocoons have a quasi-parabolic shape, from the jet-head down to the point where the cocoon reaches a maximum width. At larger distances from the jet-head (closer to the jet inlet), the width of the cocoon slightly decreases. The simulations show that the pressure in the cocoon near the jet-head is somewhat higher than the pressure at larger distances from the jet-head. The associated pressure gradient causes the gas within the cocoon to accelerate in the direction away from the jet-head. However, at large distances from the jet head, this effect is no longer seen. If we had chosen reflective boundary conditions, instead of free outflow boundary conditions, then this would have lead to a pile up of cocoon material near the lower boundary, leading to a broader cocoon base. Therefore, we note that the decrease in cocoon width near the jet inlet might just be a boundary effect.

Overall, the isothermal jet has the broadest cocoon. The heads of the jets show clear differences between the individual models: The jet-heads of the isothermal and isochoric jets have a wide and round shape (see contour plots 7 (**B** and **C**) and for a blow-up of the jet-head 6 (**B** and **C**). The homogeneous jet, on the other hand, shows a sharply peaked jet-head (see 7 **A** and 6 **A**).

4.9 Density distribution within the cocoons

The cocoons can be divided into three regions: The first region is the outermost part of the cocoon, which we denote by R_1. This region consists of pure shocked ambient medium and is found between the outer edge (bow-shock) of the cocoon and the yellow contour that encloses jet material. The other two regions R_2 and R_3 both contain shocked jet material. We denote the inner part of the cocoon by R_3, the part where most of the shocked jet material is flowing down the cocoon. Finally, there is a transition layer between the regions R_1 and R_3, which we denote by R_2.

The number density in the region R_1 is typically on the order of $n \sim 4-5\ n_{\rm ch}$ (where we initiated $n_{\rm am} = n_{\rm ch} = 10^{-3}$ cm^{-3}). The compression ratio, which can be calculated from shock conditions in the case of a strongly shocked non-relativistic gas ($\Gamma = 5/3$) takes the value $r = \frac{\Gamma+1}{\Gamma-1} = 4$. In case of a relativistically hot gas ($\Gamma = 4/3$), the compression ratio will be $r = 7$ [18]. Since we are dealing with a polytropic index, based on a Synge-like equation of state which interpolates between these two values, and the fact that this shocked ambient medium has a polytropic index slightly less than 5/3, a compression ratio slightly higher than 4 is expected.

In the region R_2, the shocked jet material has undergone strong mass-weighted mixing with the shocked ambient medium. The typical number density in this region is on the order of $n \sim 10^{-2}\ n_{\rm ch}$. As a practical definition we define region R_2 by the condition $\Lambda \geqslant 0.01$, where Λ is the mass-weighted mixing between (shocked) jet material and shocked ambient medium, defined in equation (47).

The innermost region R_3 mostly consists of shocked jet material and contains a small amount of shocked ambient medium material. This region R_3 contains material with the lowest density within the cocoon which is typically $\sim 10^{-3}\ n_{\rm ch}$. We define this region by the condition $\Lambda < 0.01$, but the values tend to become very small (typically $\Lambda \leqslant 10^{-4}$).

4.10 Distribution of relativistic gas

In all three models, the effective polytropic index tends to obtain its lowest values (and therefore becomes more relativistically hot) at the innermost part of the cocoon, region R_3, where the mass densities are low. Most relativistic gas is found near the jet-head, where the jet material has just gone through the Mach disk. It gradually becomes less relativistic with increasing distance from the jet-head. This is due to the expansion and associated cooling of the material.

To distinguish those regions that are relativistically hot, we look for gas with $\Gamma_{\rm eff} \leqslant 1.417$ (the green contour in the contour plots 7 **A, B**, and **C**). As can be seen in these contour plots, there are two distinct regions that are relativistically hot. The first is a very thin region found at the interface between jet and cocoon, near the jet inlet and might be caused by spurious effects in the lower boundary cells, next to the jet inlet. The second region containing relativistic gas is at the jet-head where the jet flow is terminated and goes through the Mach disk. This is also seen in line plots 2 and 4 (**A, B** and **C**), where the gas becomes relativistically hot when the temperature rises up to $T \sim T_{\rm ch}$. This relativistically hot region corresponds to the hot spot of the jet. The hot spot of the $H1$ jet has an elongated shape, whereas the $I1$ and $A1$ jets show a concave (bowl) shape that has a dip near the jet's centre. In section 5.2, we will discuss the morphology of the U-shaped hot spot in more detail.

[18] The simulations show that the cocoons expand with sub-relativistic velocities, which allow us to consider these expressions for the compression ratio. In case of shocks propagating at relativistic speeds, the compression ratio will also depend on the Lorentz factor (see for instance van Eerten et al. 2010).

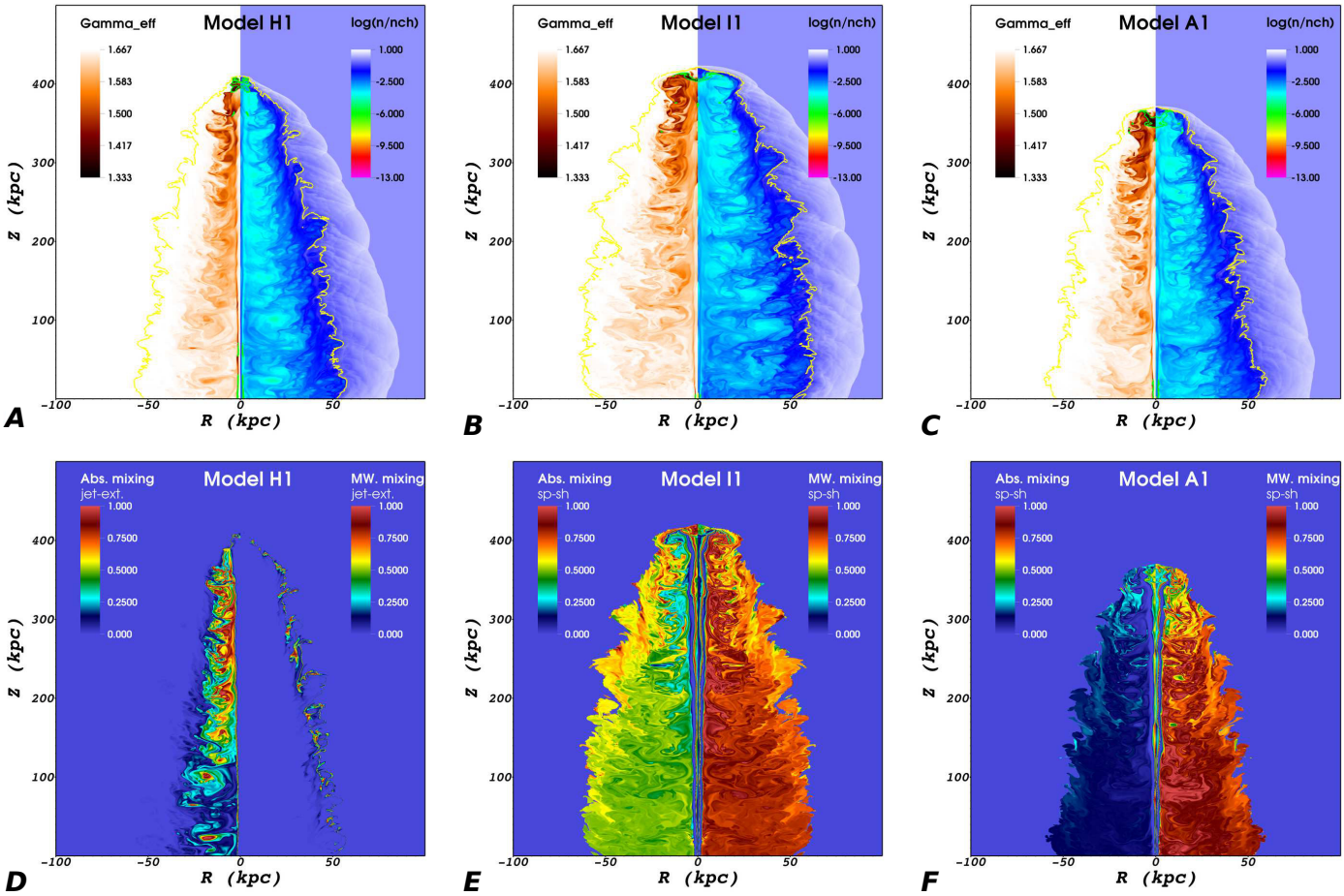

Figure 7. Contour plots of the homogeneous jet ($H1$, panels on the left hand side), the isothermal jet ($I1$, centre panels) and the isochoric jet ($A1$, panels on the right hand side) after 22.8 Myr. Note: the $R-$axis has been stretched by a factor of 2.5 in order to enhance the visibility of the actual jet behavior.
Contour plots (A, B and C) show the effective polytropic index $\Gamma_{\rm eff}$ (left hand side of the plots) and the $\log_{10}$ of the number density in terms of the characteristic number density $n_{\rm ch} = 10^{-3}{\rm cm}^{-3}$ (right hand side of the plots). The yellow contour marks the boundary where jet material (shocked, as well as unshocked) is found. The green contour (mainly found at the jet-head) encloses relativistic gas with $\Gamma_{\rm eff} \leqslant 1.417$.
Contour plots (D, E and F) show the absolute mixing (Δ) on the left side of the plots and the mass-weighted mixing (Λ) on the right side of plots. For the homogeneous jet ($H1$), the mixing between (shocked) jet material and shocked ambient medium (denoted as "ext") is shown, as described by equations (45) and (47). For the isothermal jet ($I1$) and the isochoric jet ($A1$), absolute mixing $\Delta_{\rm sp-sh}$ and mass-weighted mixing $\Lambda_{\rm sp-sh}$ between (shocked, as well as unshocked) spine material and sheath material is shown, as described by equations (43) and (46).

4.11 Mixing effects in the cocoons

Since we are dealing with a structureless homogeneous jet, as well as with jets with a spine-sheath jet structure, we can consider different kinds of mixing effects. The $H1$ jet only consists of a single jet constituent, so we shall consider the mixing between this (shocked, as well as unshocked) jet material and the shocked ambient medium. The $I1$ and $A1$ jets have a spine-sheath jet structure. There, we will be concerned with the internal mixing between jet spine and jet sheath material within the jet itself, as well as the mixing between shocked (spine and sheath) jet material in the surrounding cocoon. We shall consider each individual model separately.

4.11.1 Mixing in the cocoon for the homogeneous jet model $H1$

Contour plot 7 **D** shows the absolute and mass-weighted mixing factors Δ and Λ between jet material and shocked ambient medium. A very thin layer of strongly mixed material resides along the jet's boundary and persists all the way up to the jet's head.

Moreover, strong absolute mixing is found in the inner region of the cocoon where the densities are low ($n \sim 10^{-3}\ n_{\rm ch}$). In these regions, the mass fractions of shocked ambient medium material and jet material are nearly equal. However, outside the yellow contour marking the boundary between shocked jet and shocked ambient, densities of the shocked ambient medium are on the order of $\sim 4\ n_{\rm ch}$. Therefore, regions that contain strongly mixed material only contain a tiny fraction of the available amount of shocked ambient medium ($\sim 0.1 - 1\%$). This is also reflected in the behavior of the mass-weighted mixing. It shows that virtually no mass-weighted mixing takes place in the inner region of the cocoon, $\Lambda \leqslant 10^{-4}$. Only very thin filaments of (mass-weighted) well-mixed material are found adjacent to the yellow contour, where the two constituents are in close contact.

4.11.2 Mixing in the cocoons for the spine-sheath jet models

Contour plots 7 (**E** and **F**) show the mixing factors $\Delta_{\rm sp-sh}$ and $\Lambda_{\rm sp-sh}$ between spine and sheath material as it occurs within the jet, as well as in the surrounding cocoon. All mixing takes place within the yellow contour shown in contour plot in figures 7 **B** and 7 **C** respectively. As soon as the jet material has crossed the Mach disk, the shocked spine and sheath material have already mixed by a considerable amount. This shocked spine and shocked sheath material continues to mix further as one moves back away from the jet-head due to the effect of vortices and turbulent flows.

4.11.3 Shocked spine and sheath mixing: the isothermal jet $I1$

For the $I1$ jet, the absolute mixing factor $\Delta_{\rm sp-sh}$ in the cocoon is strongest near the jet-head, where absolute mixing $\Delta_{\rm sp-sh} \sim 1$. Here, the largest variations in mixing occur, and with increasing distance from the jet-head, the absolute mixing saturates towards a fairly homogeneous state of $\Delta_{\rm sp-sh} \sim 0.5$ at the lower regions of the cocoon.

The mass-weighted mixing $\Lambda_{\rm sp-sh}$ for the $I1$ jet, on the other hand, shows that near the jet's head, the shocked spine and shocked sheath material in the cocoon have mixed to some extent, but the amount of mass-weighted mixing varies largely near the vortices. The mixing increases with increasing distance from the jet-head. Strong vortices are found close to the jet axis, where the mass-weighted mixing approaches $\Lambda_{\rm sp-sh} \longrightarrow 1$. Most vortices have dissolved at distances larger than 291 kpc from the jet-head. There, the mixture has become fairy homogeneous with mass-weighted mixing approaching $\Lambda_{\rm sp-sh} \sim 0.8 - 1$.

4.11.4 Shocked spine and sheath mixing: the isochoric jet $A1$

In contrast to the isothermal jet, the absolute mixing in the cocoon of the isochoric $A1$ jet is fairly weak (see contour plot 7 **F**). Even at the jet-head, the absolute mixing hardly exceeds $\Delta_{\rm sp-sh} = 0.5$. As soon as shocked jet material starts to flow away from the jet-head, the absolute mixing quickly drops down to $\Delta_{\rm sp-sh} \sim 0.1$ and becomes a fairly homogeneous mixture at distances larger than 100 kpc from the jet-head. The main reason that the absolute mixing for the $A1$ jet is weaker than the absolute mixing for the $I1$ jet is the fact that the density contrast between jet spine and jet sheath for the $A1$ jet is larger than that of the $I1$ jet.

The fact that absolute mixing does not always give the correct intuitive sense for the amount of homogeneity is well reflected in the right panel of contour plot 7 **F**, where the mass-weighted mixing shows a completely different picture of the amount of mixing. Material that crosses the Mach disk is weakly mixed, but as the jet material flows back into the cocoon, filaments of strongly mixed material ($\Lambda_{\rm sp-sh} \sim 1$) are carried along by vortices and turbulent flows. These regions of strong mass-weighted mixing increase in size and moving down the cocoon, the jet material saturates to a fairly homogeneous mixture, attaining values of $\Lambda_{\rm sp-sh} \sim 0.9$ - 1.

4.12 Cocoon-jet coupling

At the jet-head, where the jet impacts the ambient medium, a complex structure of flow lines forms (see figures 6 **A, B** and **C**). When the jet flow is terminated at the Mach disk, and material is deflected away from the jet-head into the cocoon, vortices will form. These vortices are able to reside at the jet-head for a certain amount of time, but eventually they will break off the jet-head structure and move down the cocoon, entrained by mainly shocked back-flowing

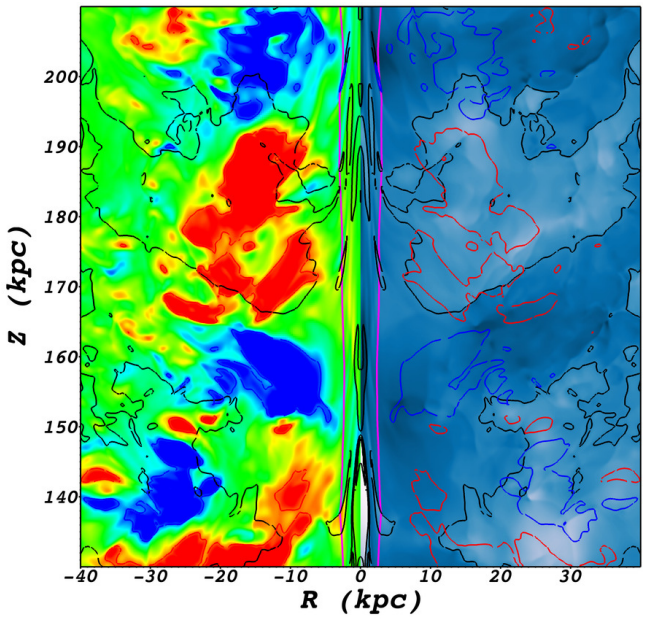

Figure 8. A close up of the isothermal ($I1$) jet in direct contact with the surrounding cocoon. It shows the connection between internal shocks within the jet (shown by the black contours along the jet centre) and vortices in the cocoon. The pink contour from the centre bottom to the centre top of the plot marks the boundary of the jet. **Left panel**: The red-green-blue color scale denotes the velocity of gas in the *radial direction*. The *red* regions mark gas that is moving away from the jet and *blue* regions mark gas that is moving towards the jet. The red and blue contours (left and right panel) denote material moving with $V_{\rm R} = \pm 0.08c$ respectively. **Right panel:** The gray-blue color scale denotes the ($\log_{10}$ of the) gas pressure of the cocoon and jet material. Darker regions correspond to higher pressure. High pressure regions compress the jet and cause internal shocks to emerge. These high pressure regions correlate with gas moving towards the jet, whereas low pressure regions correlate with gas moving away from the jet.

jet material. After a vortex is shed by the jet-head, a new vortex starts to form and the cycle repeats itself.

The shed vortices are advected down the cocoon and create pressure waves within the cocoon. Figure 8 shows a close up of part of the $I1$ jet, denoted by the pink contour, and its surrounding cocoon. The left panel of the plot shows the radial velocity component $V_{\rm R}$. The red regions are moving away from the jet ($V_{\rm R} > 0$) and the blue regions are moving towards the jet ($V_{\rm R} < 0$). The alternating pattern in radial velocity that emerges is caused by the train of vortices that have broken off the jet-head in a quasi-periodic and regular way. The right panel shows the ($\log_{10}$) of the gas pressure. Dark colors correspond to high pressure, and light colors to low pressure. The red and blue contours indicate radial velocity ($V_{\rm R} = \pm 0.08c$ respectively). Finally, the black contours indicate pressure with values $\log_{10}(P/P_{\rm ch}) = \{-6,\ 5.3,\ 4.7,\ -4\}$.

When we compare the right panel to the left panel in figure 8, we find that the regions of high pressure correlate well with gas moving towards the jet and that the regions of low pressure correlate with gas moving away from the jet. This means that the alternating pattern in radial velocity directly corresponds with the pressure waves traveling down the cocoon. Moreover, it can be seen that at the sites where the high pressure regions are in contact with the jet boundary, the jet is compressed, which consequently leads to the formation of a strong internal shock.

All three models show this correspondence between the for-

mation of strong internal shocks and the pressure waves caused by the back-flowing vortices. Therefore, we can directly translate the number of internal shocks along the jet axis to the number of back-flowing vortices in the cocoon. The jets $H1$, $I1$ and $A1$ all have approximately 9 internal shocks at the final time of simulation, $t = 22.8$ Myr. We find a fairly regular pattern in the pressure waves traveling down the cocoon, which points towards an approximately constant vortex cycle time, $t_{\rm vortex}$. We find $t_{\rm vortex} \sim 2.5$ Myr. With the assumption of constant vortex cycle time, we can approximate the number of shocks $N_{\rm s}$ that have formed along the jet axis, at a time t after the jet has been injected by:

$$N_{\rm s} \approx \frac{t}{t_{\rm vortex}} = 0.40\, t\,, \tag{55}$$

with t in Myr. At time t, a cocoon with length $L_{\rm co} = \beta_{\rm hd}\ t$ will have formed, where $\beta_{\rm hd}$ is the jet-head advance speed. Therefore, the relation between cocoon length and number of shocks is also given by:

$$N_{\rm s} \approx \frac{L_{\rm co}}{d_{\rm vortex}}\,, \tag{56}$$

where $d_{\rm vortex} = \beta_{\rm hd}\ t_{\rm vortex}$ is the average distance between two vortices, for which we find an average $d_{\rm vortex} \sim 44$ kpc.

One should note however that in a more realistic case where a jet is simulated in full $3D$, using magnetohydrodynamics, other types of instabilities might alter the behavior of the vortices at the jet-head. In that case, the pressure waves traveling down the cocoon might be more irregular than in case of the $2.5D$ simulations that are described in this paper so that a typical vortex cycle time might not apply. However, regardless of the type of instabilities, pressure waves are inevitably created that cause pressure fluctuations in the cocoon. An increase of cocoon pressure will lead to jet constriction and the formation of internal shocks.

5 DISCUSSION

5.1 Will the jets appear as FRI or FRII jets?

Since all three jet models $H1$, $I1$ and $A1$ have been given a typical FRII jet power ($L_{\rm jt} = 4 - 5 \times 10^{46}$ erg s^{-1}), one might expect that the jets will further evolve as FRII jets as well. Indeed, we find that global features such as the length and the width of the cocoon, the number of internal shocks along the jet axis and the stability of the jets do not show large variations between the individual models. All three jets maintain their stability all the way up to the jet head. Moreover, regions with relativistic gas are found downstream of the Mach disk which can be identified with the hot spots of the jets. Collimated and undisrupted jets with hot spots at their jet-heads are two typical signatures for FRII jets. Therefore, based on these signatures we conclude that the $H1$, $I1$ and $A1$ jets (initiated as FRII jets) will all continue to further develop as FRII jets.

5.2 Jet-head structure and the mixing of components

For the homogeneous jet, the structure of the jet-head and the general behavior of the flow lines can be fairly easily understood. As soon as it impacts the ambient medium, a bow shock and Mach disk are formed. All jet material is shocked equally strong throughout the cross section of the jet. The shocked jet material and the shocked ambient medium both have a high pressure and the associated pressure gradients cause the shocked material to flow away from the jet-head. Vortices are created in this high pressure region, which cause shocked jet material and shocked ambient medium material to mix strongly. This behavior can be seen in the flow patterns of figure 6 **A**.

For jets with structure consisting of a fast moving jet spine and slower moving jet sheath, the formation, structure, and evolution of the jet-head is more complex. In this case, the jet spine (with a higher bulk velocity) initially impacts the shocked ambient medium before the jet sheath does. Material from the jet spine will be shocked by the Mach disk and, together with the shocked ambient medium, form a preceding substructure in the jet-head. Material in this substructure flows away from the bow shock due to pressure gradients, causing turbulence and possibly vortices where shocked spine material and shocked ambient medium mix strongly.

The jet sheath, on the other hand, doesn't impact the shocked ambient medium directly, but it impacts this preceding jet-head substructure. The pressure in the preceding jet-head will be high because the Mach disk and the bow shock are both strong shocks. The shocked jet spine expands sideways after the Mach disk due to this pressure jump. Because the jet sheath has slightly higher density, but lower inertia, it can be more easily displaced than the jet spine. It is therefore pushed outwards, while still propagating towards the top of the jet-head. Further out it is deflected due to the high pressure in the preceding jet-head, causing the shocked sheath material to flow back into the cocoon. This flow pattern causes the hot spot to obtain a concave shape, which is seen in both the models $I1$ and $A1$.

The back-flowing shocked sheath creates more vortices. At these vortices, shocked spine, shocked sheath and shocked ambient medium material all mix strongly. As the vortices evolve and shocked material flows away from the jet-head, the different constituents eventually evolve into an approximate homogeneous mixture at large distances from the jet-head. Figure 8 shows vortices in the cocoon of the $I1$ jet as they are moving downstream from the jet-head. Figures 7 (**E** and **F**) show that at large distances from the jet-head, where shocked gas from the cocoon has gone through much turbulence, the mixture of shocked spine-sheath material in the cocoon has become approximately homogeneous.

5.3 Effective impact surface area of the ambient medium

Even though the assumption of using an area-weighted average for the analytical prediction of the jet-head advance speed is a rather simple one, the values obtained are remarkably close to the actual values at the start-up phase of the simulations. However, not long after this start-up phase ($\gtrsim 2.5$ Myr), we see the advance speed of the jet-heads of all three models decline to a new, fairly constant value (although the advance speed for model $I1$ continues to decline slightly during the entire run of the simulation). Taking an average over the final 2.8 Myr shows that the jet-heads only propagate with $\sim$ 15% - 25% of their initial velocity.

The total momentum discharge through the Mach disk (also see Rosen et al. 1999) is given by:

$$Q_{\rm jt} = \Big[(e + P)\,\gamma_{\rm MD}^2\beta_{\rm MD}^2 + P\Big]_{\rm jt}\ A_{\rm jt} \tag{57}$$

where as before e is the total internal energy density, P is the pressure, $\gamma_{\rm MD}$ and $\beta_{\rm MD}$ are the bulk jet Lorentz factor and velocity respectively as measured in the frame of the Mach disk, and finally $A_{\rm jt}$ is the discharge surface area of the jet. One important note must be made. The conditions in the jet, just before the Mach disk will significantly differ from those at the jet inlet. For example, the surface of the cross section of the jet will be larger; the mass density,

pressure and temperature will differ; and the velocity profile will also have changed. However, the total momentum discharge must approximately be constant at all Z, so we can safely use the parameters at jet inlet.

We explain the quickly decelerating jet-head advance speed by assuming that the impact surface area $A_{\rm jt}$ of the jet over which the momentum discharge takes place and the impact surface area of the ambient medium $A_{\rm am}$ are not equal: $A_{\rm jt} \neq A_{\rm am}$ [19]. If we take these unequal surface areas into account in equation (30), the analytical prediction for the jet-head advance speed becomes:

$$\beta_{\rm hd} = \frac{\gamma_{\rm jt}\sqrt{\eta_{\rm R}}\,\beta_{\rm jt}}{\Omega + \gamma_{\rm jt}\sqrt{\eta_{\rm R}}}\ , \tag{58}$$

where $\Omega = \sqrt{\frac{A_{\rm am}}{A_{\rm jt}}}$ is the square root of the ratio of impact surface areas. In these $2.5D$ simulations, the impact surface area of the jet is a disk $A_{\rm jt} = \pi R_{\rm jt}^2$ with radius $R_{\rm jt}$, and the impact surface area of the ambient medium is a disk $A_{\rm am} = \pi R_{\rm am}^2$ with radius $R_{\rm am}$. From this we find for the effective impact radius:

$$R_{\rm am} = \gamma_{\rm jt}\sqrt{\eta_{\rm R}}\left(\frac{\beta_{\rm jt}}{\beta_{\rm HD}} - 1\right)R_{\rm jt}\ , \tag{59}$$

where $\beta_{\rm HD}$ is now the actual measured jet-head advance speed. We substituted the results for the jet-head advance speed we found from the simulations and listed the effective impact radii in table 3. As can be seen in figure 6 (**A**, **B** and **C**), the yellow flow lines represent the effective impact radius for the three jet models. The size of the impact area corresponds very well to the (projected) size of the turbulent region of shocked gas in the jet-head (the green flow lines), and is approximately similar to the cross section of the jet, just before the Mach disk.

The effective impact area is Ω^2 times as large as in the case predicted by simple theory. This is 16 for the homogeneous jet, 30 for the isochoric jet and even 40 for the isothermal jet, which shows that AGN jets are capable of shock-heating fairly large regions of the surrounding intergalactic medium.

5.4 Jet structure and transverse jet integrity

5.4.1 *The effect of a radial variation in density $\rho(R)$ and relativistic inertia $\gamma^2\rho h(R)$*

In this section, we discuss the stability of the jet, as well as the integrity of the jet in the *radial* direction. The choice for the radial initialization of a jet strongly determines its further evolution as it propagates into the ambient medium. In particular, the difference between the three models of the radial density variation $\rho(R)$ and the relativistic inertia (perpendicular to the jet flow) $\gamma^2\rho h(R)$ play an important role. Table 4 shows the values of the density and relativistic inertia at the jet axis $R = 0$; the jet spine-sheath interface $R = R_{\rm sp}$ and the jet boundary $R = R_{\rm jt}$.

As discussed in section 4.12 on cocoon-jet coupling, pressure gradients in the cocoon surrounding the jet can cause the jet to be compressed. Such a compression causes a shock to form in the centre part of the jet (therefore, in the case of structured spine-sheath jet, in the jet spine). Such an internal shock is capable of propagating through the jet itself, in poloidal, as well as in the radial direction. After a strong internal shock has occurred in the jet centre, the post-shock jet material gets heated, causing the jet material to expand sideways. The influence of different density- and relativistic inertia variations on the propagation of such a shock, and its relation to internal mixing between jet spine and jet sheath material shall be discussed for each individual model.

The homogeneous jet ($H1$) maintains its radial integrity almost entirely up to the jet-head. At the jet head, the jet material has crossed 9 strong internal shocks, but these have not disrupted the jet flow, or lead to a large amount of mixing between jet and surrounding cocoon material. This can be explained as the result of the uniform density and Lorentz factor over the entire cross section of the jet. This leads to a uniform shock strength, and the post-shock sideways expansion of the jet material will be similar at all radii as the relativistic inertia, $\gamma^2 h\rho$ with $h \sim 1$, is constant across the entire cross section (also see tabel 4).

The absence of a radial density- and relativistic inertia variation results in a stable jet with a stable radial structural integrity (see for example line plot 4 **D** and the radial cuts in figure 5 (**A**, **B** and **C**).

The isothermal jet ($I1$) maintains a considerable amount of its radial structural integrity up to large distances from the jet inlet. Its density varies smoothly in the radial direction of the jet (see figure 1 **C**) [20]. When a shock emerges in the jet spine due to a pressure variation in the cocoon, these shocks propagate outwards. When the shock reaches the jet spine-sheath interface, the shock will not be reflected, since the density variation across this interface is zero. Moreover, the inertia of the jet sheath is a factor 4 less than that of the jet spine (see table 4). Therefore, the jet sheath will easily be deflected outwards by the shock-heated jet spine material.

The absence of shock reflections at the jet spine-sheath interface, together with a jet sheath that has lower relativistic inertia than the jet spine yield inefficient internal mixing between the jet spine and jet sheath material. Therefore, a considerable amount of the radial structural integrity will be maintained up to large distances from the jet inlet. This behavior can be seen in line plot 4 **E** and from the radial cuts in figure 5 (**D**, **E** and **F**).

The isochoric jet ($A1$) loses its radial structure fairly quickly after the jet is injected into the system. As with the isothermal jet, shock develop in the jet spine and propagate outwards. However, in this case, when such a shock reaches the jet spine-sheath interface, the shocks are largely reflected because of a jump in density by a factor of 5 in jet sheath. Moreover, the jet sheath has slightly higher relativistic inertia than the jet spine, which enhances the effect of the shock reflections (see table 4). Each internal shock reflection internally mixes the jet spine and jet sheath more, and therefore soon after inlet, the clear spine-sheath jet structure will be lost. This behavior can be seen in line plot 4 **F** and the radial cuts in figure 5 (**G**, **H** and **I**).

The relation between shock reflections and internal jet spine-sheath mixing is explained as follows: Flow lines that cross a shock are deflected away from the shock normal. Such a deflection will

[19] There is also a small fraction of ambient medium material entrained by the jet. However, this fraction is so small ($\sim 1\%$), we expect this effect not to influence the deceleration of the jet.

[20] Note that this is a consequence of choosing the isothermal jet to have a constant temperature across the entire jet cross section.

Table 4. Variation of density and relativistic inertia for the jets $H1$, $I1$ and $A1$, in the radial direction.

Quantity ($10^{-3} m_{\rm p} n_{\rm ch}$)	**at radius**	**H1**	**I1**	**A1**
Density ρ	$R = 0$	4.55	3.31	1.00
	$R = R_{\rm sp}^{-}$	4.55	4.89	1.00
	$R = R_{\rm sp}^{+}$	4.55	4.89	5.00
	$R = R_{\rm jt}$	4.55	5.00	5.00
Rel. inertia $\gamma^2 \rho h$	$R = 0$	44.1	119.0	36.0
	$R = R_{\rm sp}^{-}$	44.1	176.0	36.0
	$R = R_{\rm sp}^{+}$	44.1	44.0	45.0
	$R = R_{\rm jt}$	44.1	45.0	45.0

Table showing the density ρ and the relativistic inertia $\gamma^2 \rho h$ of the initial radial jet profile, both in units of $10^{-3} m_{\rm p} n_{\rm ch}$, at different distances from the jet axis: $R = 0$ corresponds to the jet axis; $R = R_{\rm sp}^{-}$ corresponds to the point just inside of the jet spine-sheath interface; $R = R_{\rm sp}^{+}$ corresponds to the point just outside of the jet spine-sheath interface; and finally $R = R_{\rm jt}$ corresponds to the jet boundary.

create vorticity in the jet flow. A shock front that encounters a medium with a higher density (as is the case for the jet spine-sheath interface of the isochoric jet) will partially be reflected and partially be transmitted. A higher density contrast will result in a larger part of the shock being reflected. Near such a shock reflection, the creation of vorticity will be strong due to the strong deflection of the flow lines. At the interface between jet spine and jet sheath, vorticity is directly responsible for the mixing of the jet constituents. Moreover, the emergence of vorticity at the jet spine-sheath interface is capable of triggering the Kelvin-Helmholtz instability. This instability itself creates vorticity and will eventually lead to a turbulent flow.

Therefore, it is expected that the internal mixing between the jet spine and the jet sheath in jets with a large density jump across the jet spine-sheath interface will be stronger than in the case where this density jump is small, or non-existent.

5.4.2 *Critical azimuthal velocity*

Regardless of the physical mechanism (for example, constant angular velocity Ω, or constant specific angular momentum λ) that eventually leads to a certain amount of rotation at a certain distance from the central engine, there is another physical restriction that determines an upper-limit for the amount of rotation, the so-called *critical azimuthal velocity*, $V_{\phi,\rm C}$. The critical azimuthal velocity follows from demanding the gas pressure on the jet axis to remain positive, $P(R = 0) \geqslant 0$.

In case of the isothermal jet, we derived in section 2.4.1 that this translates into the condition $V_\phi < \sqrt{1 - V_z^2}$. Since the jet spine of the structured jets has a Lorentz factor $\gamma_{\rm sp} = 6$, the critical azimuthal velocity of the isothermal jet equals $V_{\phi,\rm C}^{\rm I} = 0.167$.

The condition for the pressure to remain positive on the jet axis in case of the isochoric jet (section 2.4.2), leads to an expression that cannot be solved analytically. We have made a second-order Taylor expansion in $(\Delta V^2) = V_\phi^2 - V_{\phi,0}^2$ for this expression to obtain an accurate value for the critical azimuthal velocity. Here, the value of $V_{\phi,0}$ is assumed to lie close to the true value of the critical azimuthal velocity. We determined the critical azimuthal velocity for the isochoric jet to be: $V_{\phi,\rm C}^{\rm A} = 3.159 \times 10^{-3}$.

Figure 9 (**A**, **B**, **C** and **D**) shows the initial radial jet profiles for both the isothermal jet, as well as the isochoric jet as they would appear for a critical azimuthal velocity $V_\phi = V_{\phi,\rm C}^{\rm A} = 3.159 \times 10^{-3}$. Clear differences can be seen between these radial jet profiles, and the ones shown in figure 1 (**A**, **B**, **C** and **D**), especially in the jet spine region.

Our choices for the self-similarity constants $a_{\rm sp}$ and $a_{\rm sh}$ have been discussed in section 2. We chose the self-similarity constant in the jet sheath $a_{\rm sh} = -2$, motivated by constant specific angular momentum. The self-similarity constant of the spine needs to be positive, however, its choice $a_{\rm sp} = 1/2$ was somewhat arbitrary. The criterion for internal stability ($\{a_{\rm sp}, a_{\rm sh}\} > -2$) does, however, allow for different values for $a_{\rm sp}$ and $a_{\rm sh}$. For completeness' sake, the authors have studied the effect of choosing different sets $\{a_{\rm sp}, a_{\rm sh}\}$ on the initial radial jet profiles. It turns out that with the present choice of the maximum azimuthal velocity, V_ϕ, different (but still realistic) values for $\{a_{\rm sp}, a_{\rm sh}\}$ do not strongly influence the resulting radial jet profiles, for both the isothermal jet, as well as for the isochoric jet. We therefore argue that with our present choice, $a_{\rm sp} = 1/2$; $a_{\rm sh} = -2$ and $V_\phi = 1 \times 10^{-3}$, the resulting jet profiles should be representative for the actual isothermal and isochoric jets, even in the case where the actual self-similarity constants of the jets differ (modestly) from the values that were used in this paper. These specific jet models are relatively insensitive to different choices for $\{a_{\rm sp}, a_{\rm sh}\}$.

However, strong responses to the choice of $\{a_{\rm sp}, a_{\rm sh}\}$ do occur as one lets the maximum azimuthal velocity approach the critical azimuthal velocity. For a more complete understanding of both the fundamental properties of, as well as the fundamental differences between the isothermal and isochoric jet models (for example looking at mixing effects and jet integrity), the case where the maximum azimuthal velocity constant approaches the critical azimuthal velocity, $V_\phi \longrightarrow V_{\phi,\rm C}$, should be studied as well.

5.4.3 *The effect of cylindrical symmetry on mixing effects*

As a last note, it needs to be mentioned that the amount of mixing presented in this paper should be taken with some caution. Performing simulations in axisymmetric 2.5D models has the advantage of producing "some aspects" of 3D behavior, while keeping the amount of computation time manageable. However, in full 3D, in addition to the type of instabilities that occur in this 2.5D study, also different kind of instabilities will occur, which will automatically lead to more turbulence and possibly less stable jets. As we discussed, turbulence is the primary mechanism behind the amount of mixing (along the jet axis, as well as in the surrounding cocoon). It is therefore expected that 2.5D models likely give an underestimation as compared to the amount of mixing that would occur in full 3D simulations.

6 CONCLUSIONS

In this paper, we compared three different AGN jet models with a jet power of $L_{\rm jt} \sim 4 - 5 \times 10^{46}$ erg s^{-1}, a typical energy for powerful FRII radio sources. We simulated a homogeneous jet (denoted as $H1$) without radial structure or angular momentum, and two different jet models with a radial spine-sheath jet structure carrying angular momentum. For both spine-sheath jets, the jet spine has lower mass density and higher Lorentz factor than the jet sheath. The first spine-sheath jet (denoted as $I1$) is a jet set up with an isothermal equation of state. The second spine-sheath jet (denoted

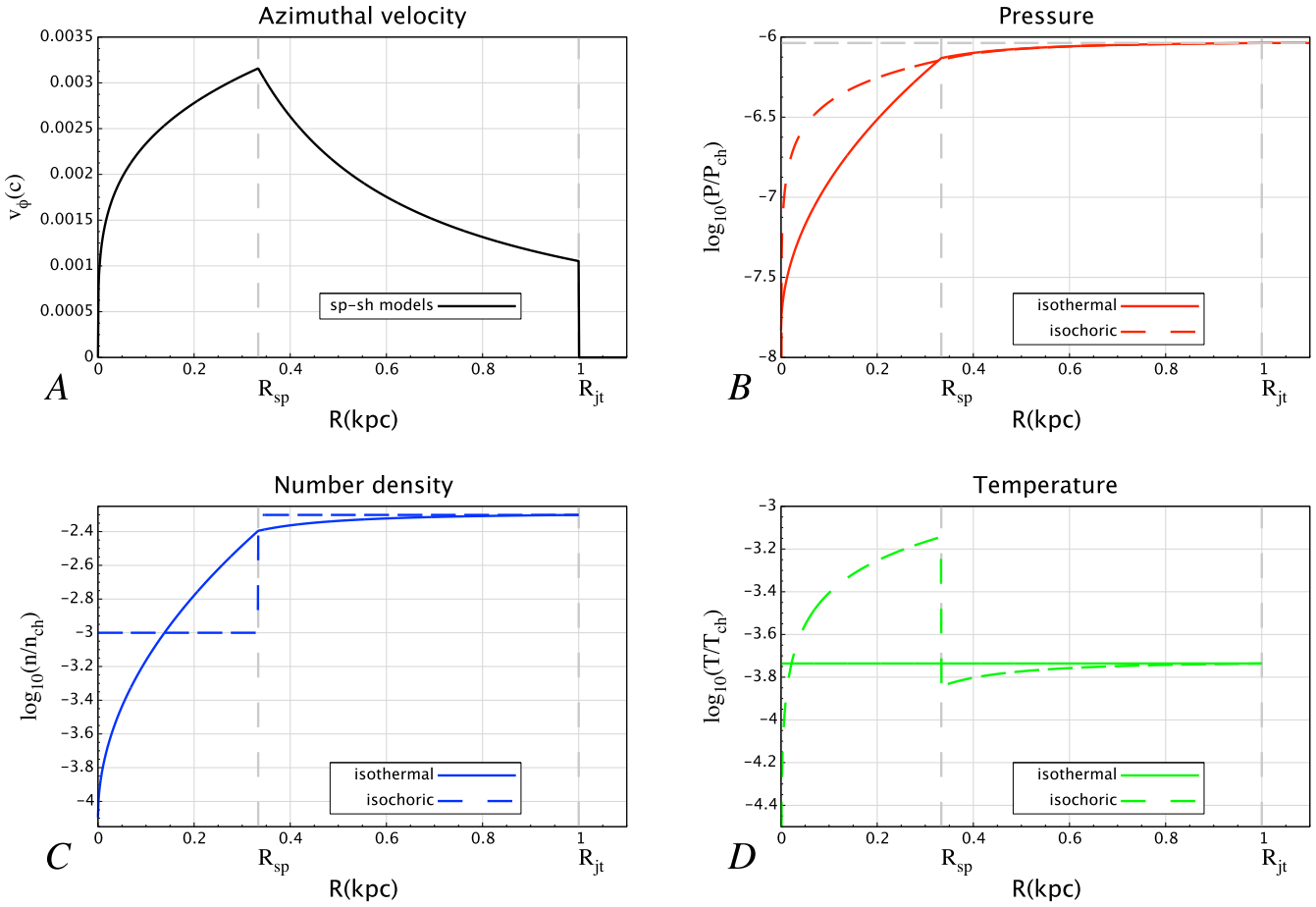

Figure 9. Initial transverse jet profiles for the isothermal jet (solid lines) and the piecewise isochoric jet (dashed lines), *but now in the case of* $V_\phi = V^{\rm A}_{\phi,{\rm C}} = 3.159 \times 10^{-3} c$. The cross cuts show in *black* the profile of azimuthal rotation $v_\phi(R)$ (figure **A**). This rotation profile has been used for both the isothermal and the isochoric jet model; In *red*, the $\log_{10}$ of the pressure P in units of the characteristic pressure $P_{\rm ch} = 1.50 \times 10^{-6}$ erg cm^{-3} (figure **B**); In *blue* the $\log_{10}$ of the number density n in units of the characteristic number density $n_{\rm ch} = 10^{-3}$ cm^{-3} (figure **C**); and in *green* the $\log_{10}$ of the thermal temperature T in units of the characteristic temperature $T_{\rm ch} = 1.09 \times 10^{13}$ K (figure **D**) of the jet. In addition, the images show the jet radius at $R_{\rm jt} = 1$ kpc and the jet spine radius at $R_{\rm sp} = R_{\rm jt}/3$ as the two vertical dashed lines. The pressure of the ambient medium is denoted by the dashed horizontal line in figure **B**.

as $A1$) is a (piecewise) isochoric jet: set up with constant, but different density for jet spine and jet sheath, using a polytropic index of $\Gamma = 5/3$.

We simulate these jets in the case of a steady scenario where the jets have been active for 22.8 Myr. The jets are under-dense as compared to the ambient medium by a factor of $\eta \sim (1-5) \times 10^{-3}$. All three jet models reach approximately the same distance of 400 kpc, where the individual models differ by a few tens of kpc. At the final time of simulation, all three jets have developed approximately 9 strong internal shocks. The emergence of these shocks can be directly linked to the shedding of vortices by the jet-head, causing pressure waves to travel down the cocoon and compress the jet at the high pressure regions. At the Mach disk, all three jets are shocked to relativistic temperatures. This relativistically hot gas is identified with the hot spot of the jet. Based on the stability of the jets and the appearance of hot spots, we conclude that all three jets will have developed as typical FRII jets.

We find that the homogeneous jet ($H1$) remains regular all the way up to the jet-head with the same Lorentz factor as it was initiated at the jet inlet. It has an elongated hot spot and a fairly flat Mach disk.

The isothermal jet ($I1$) loses its structural integrity slowly with increasing distance from the jet inlet. However, all the way up to the jet-head, the core of the jet is still predominantly made up of jet spine material and the surrounding layer still consists predominantly of jet sheath material. The Lorentz factor of the central part of the jet is still slightly higher than that of the surrounding jet sheath. Due to the fact that the density contrast between jet spine and jet sheath is zero at the jet spine-sheath interface, strong internal shocks are *not* reflected at this interface. Instead, shock-heated jet spine material merely displaces the jet sheath outwards. This causes the jet spine and the jet sheath to internally mix relatively *inefficient* within the isothermal jet.

The isochoric jet ($A1$) loses most of its structural integrity after the jet is injected into the system. After crossing two strong internal shocks, the central part of the jet is dominated by jet sheath material and the Lorentz factor is only slightly higher than that of the surrounding jet sheath. At the jet-head, the jet spine material has been smeared out over a large part of the jet cross section and there is only a thin outer region that is still made up predominantly of jet sheath material. This difference is caused by a strong jump in density at the interface between the jet spine and the jet sheath.

Table 5. Summary of the most appreciable characteristics of the three jet models $H1$, $I1$ and $A1$.

Jets at t = 22.8 Myr	**Homogeneous H1**	**Isothermal I1**	**(Piecewise) isochoric A1**
Jet length	*409 kpc*	*421 kpc*	*370 kpc*
Maximum cocoon width	*85 kpc*	*90 kpc*	*86 kpc*
Appearance hot spot	*elongated*	*concave (bowl) shape*	*concave (bowl) shape*
Internal shocks along jet axis	*9*	*9*	*9*
Appearance internal shocks	*single peaks in density and temperature*	*single peaks in density and temperature, followed by variable behavior*	*single peaks in density and temperature, followed by weaker shocks*
Jet-head	*sharply peaked*	*wide round shape*	*wide round shape*
Temperature of the Mach disk (on the jet axis)	9.7×10^{12} *K (relativistic)*	1.4×10^{13} *K (relativistic)*	1.1×10^{13} *K (relativistic)*
Mixing within the cocoon	*shocked jet- shocked ambient medium: large region of strong absolute mixing, but only little mass-weighted mixing. Far from a homogeneous mixture*	*shocked spine - shocked sheath: considerable mixing within entire cocoon Approximately homogeneous mixture for distances larger than 291 kpc from jet-head with* $\Lambda_{\mathrm{sp-sh}} \sim 0.8 - 1$	*shocked spine - shocked sheath: considerable mixing within entire cocoon Approximately homogeneous mixture for distances larger than 100 kpc from jet-head with* $\Lambda_{rmsp-sh} \sim 0.9 - 1$
Mixing along jet axis	*jet-shocked ambient medium: No notable mixing along entire axis, except at the jet-head*	*jet spine - jet sheath: considerable absolute mixing* ($\Delta_{\mathrm{sp-sh}} < 0.5$)*, but weak mass-weighted mixing* ($\Lambda_{\mathrm{sp-sh}} < 0.1$)*. Predominantly jet spine material along jet axis*	*jet spine - jet sheath: strong absolute mixing* ($\Delta_{\mathrm{sp-sh}} > 0.5$)*, and notable mass-weighted mixing* ($\Lambda_{\mathrm{sp-sh}} < 0.3$)*. Predominantly jet sheath material along jet axis for* $Z > 82$ *kpc*
Radial jet structure before hot spot	*jet integrity maintained all the way up to the hot spot*	*jet spine-sheath structure can still be recognized through the abundance of the constituents in radial direction*	*jet spine-sheath structure can no longer be recognized*
Jet-head advance speed after start-up phase	*0.047 c*	*0.032 c*	*0.035 c*

The left column contains some of the characteristic features that have been discussed in the previous sections. The second column shows these characteristics for model $H1$, the third for model $I1$ and the right column for model $A1$.

Shocks that occur within the jet spine are reflected as soon as they encounter this jet spine-sheath interface. Every shock reflection (internally) mixes the jet spine and jet sheath material further. This causes *efficient* internal mixing between jet spine and jet sheath material in the isochoric jet.

Both the isothermal jet and the isochoric jet have a concave (bowl-shaped) hot spot. This is explained by considering the complex flow behavior at the jet-head. For both structured jets we find that at each strong internal shock, only the central part of the jet is shocked and that the jet sheath merely is radially deflected by the shock-heated jet spine material. Therefore, at the jet-head, the jet sheath is not terminated at the Mach disk, but continues to propagate further towards the top of the jet-head. Then, at some point the pressure at the jet's head becomes large enough to deflect the jet sheath, from which point on it moves further down the cocoon, away from the jet-head. This flow pattern of jet sheath material deforms the hot spot, giving it the concave shape.

Finally, we find that the propagation speed of the jet-heads is less than predicted from simple theory. We find that this is most probably caused by an enlarged, effective impact area of the ambient medium that interacts with the jet. Taking this effect into account, we find that the effective impact area varies from being 16 times as large (in case of the homogeneous jet), to 30 times as large (in case of the isochoric jet) and can be up to 40 times as large (as in the case of the isothermal jet). The size of this effective impact area corresponds well to the size of the hot spots and the vortices (projected on the plane perpendicular to the jet axis) that make up part of the jet-head.

Since the homogeneous jet, the isothermal jet and the isochoric jet were all given the same jet power, and in addition there were merely subtle differences in the radial pressure- and density profiles of the two structured spine-sheath jets, we consequently found that a number of aspects of the jets and the cocoons (e.g. cocoon length and width, number of internal shocks, temperature along the jet axis and the occurrence of an enlarged effective impact area) are fairly similar. Regarding jet integrity, jet-head morphology and internal mixing efficiency between the jet spine and the jet sheath, on the other hand, we found prominent differences (see table 5 for the most notable features). It is therefore expected that with increasing difference in parameters between the individual models (such as maximum azimuthal velocity, or density contrasts), more prominent distinctive features will occur. The influence of radial jet stratification on jet integrity, jet-head morphology and the development of internal shocks have become apparent. They should therefore be taken into account when one tries to model jets in realistic scenarios.

6.1 Continuation of this work

In order to investigate the differences between the individual models further, different parts of parameter space need to be considered. For example, close to the central engine, the density contrast

between a jet spine and jet sheath, (maximum) azimuthal velocity, or Lorentz factors might be much higher and there the influence of magnetic fields should be involved as well. Another example of where other parts of parameter space apply is in the case of jets coming from micro-quasars. Moreover, in the case where the central engine shows episodic behavior (multiple subsequent outbursts), the properties of the ambient medium into which the jets are injected changes dynamically. It is expected that this changing environment will have large consequences for the jet propagation, jet stability and jet integrity. Comparing the isothermal jet model to the isochoric jet model for these other cases might lead to new insights. An extension to the work done by Meliani & Keppens (2009), where the evolution of the cross section of an isochoric jet was described, might also be performed in case of the isothermal jet model. A useful question would be if the relativistically enhanced, rotation-induced Rayleigh-Taylor instability leading to internal mixing of jet spine and jet sheath material (in cases where cylindrical symmetry no longer applies), will also occur in the isothermal jet model. Eventually simulating these models in 3D might yet reveal more fundamental differences and characteristics (as for example in mixing effects) of the different jet models.

In the follow-up of this paper we will be concerned with the case of episodic activity. Again we will compare the homogeneous jet, the isochoric jet and the isothermal jet. There we will also be concerned with jet stability and jet integrity; jet-head advance speed; effective impact area; and mixing effects of (shocked, as well as unshocked) spine and sheath material, between spine and sheath coming from the same outburst episode, as well as mixing of components coming from different outbursts.

ACKNOWLEDGEMENTS

This research is funded by the *Nederlandse Onderzoekschool Voor Astronomie* (NOVA). S.M. also acknowledges support from The European Communities Seventh Framework Programme (FP7/2007-2013) under grant agreement number ITN 215212 Black Hole Universe; Z.M. acknowledges financial support from the PNHE; and R.K. acknowledges financial support from FWO-Vlaanderen, project G.02308.12.

REFERENCES

Aloy M.-A., Gómez J.-L., Ibáñez J.-M., Martí J.-M., Müller E., 2000, ApJ, 528, L85
Begelman M. C., Blandford R. D., Rees M. J., 1984, Reviews of Modern Physics, 56, 255
Begelman M. C., Cioffi D. F., 1989, ApJ, 345, L21
Blandford R. D., Payne D. G., 1982, MNRAS, 199, 883
Blandford R. D., Rees M. J., 1974, MNRAS, 169, 395
Blandford R. D., Znajek R. L., 1977, MNRAS, 179, 433
Blumenthal G. R., Mathews W. G., 1976, ApJ, 203, 714
Bosch-Ramon V., Perucho M., Barkov M. V., 2012, A&A, 539, A69
Ciotti L., Ostriker J. P., 2007, ApJ, 665, 1038
Daly R. A., 1990, ApJ, 355, 416
Davé R., Cen R., Ostriker J. P., Bryan G. L., Hernquist L., Katz N., Weinberg D. H., Norman M. L., O'Shea B., 2001, ApJ, 552, 473
Davé R., Oppenheimer B. D., Katz N., Kollmeier J. A., Weinberg D. H., 2010, MNRAS, 408, 2051
Doeleman S. S., Fish V. L., Schenck D. E., Beaudoin C., Blundell R., Bower G. C., Broderick A. E., Chamberlin R., Freund R., Friberg P., Gurwell M. A., Ho P. T. P., Honma M., Inoue M., Krichbaum T. P., et al. 2012, Science, 338, 355
Fabian A. C., 2012, ARA&A, 50, 455
Fanaroff B. L., Riley J. M., 1974, MNRAS, 167, 31P
Ghisellini G., Tavecchio F., Chiaberge M., 2005, A&A, 432, 401
Gilkis A., Soker N., 2012, arXiv:1205.3571)
Giroletti M., Giovannini G., Feretti L., Cotton W. D., Edwards P. G., Lara L., Marscher A. P., Mattox J. R., Piner B. G., Venturi T., 2004, ApJ, 600, 127
Gitti M., Brighenti F., McNamara B. R., 2012, Advances in Astronomy, 2012
Gómez J. L., Agudo I., Marscher A. P., Jorstad S. G., Roca-Sogorb M., 2008, Mem. Soc. Astron. Italiana, 79, 1157
Hada K., Doi A., Kino M., Nagai H., Hagiwara Y., Kawaguchi N., 2011, Nature, 477, 185
Hardee P., Mizuno Y., Nishikawa K.-I., 2007, Ap&SS, 311, 281
Ito H., Kino M., Kawakatu N., Isobe N., Yamada S., 2008, ApJ, 685, 828
Keppens R., Meliani Z., van Marle A. J., Delmont P., Vlasis A., van der Holst B., 2012, Journal of Computational Physics, 231, 718
Kunz M. W., Schekochihin A. A., Cowley S. C., Binney J. J., Sanders J. S., 2011, MNRAS, 410, 2446
Leahy J. P., Muxlow T. W. B., Stephens P. W., 1989, MNRAS, 239, 401
Lobanov A. P., 2011, Mem. Soc. Astron. Italiana, 82, 33
Ma M.-L., Cao X.-W., Jiang D.-R., Gu M.-F., 2008, Chinese J. Astron. Astrophys., 8, 39
Marti J. M. A., Mueller E., Font J. A., Ibanez J. M. A., Marquina A., 1997, ApJ, 479, 151
Meliani Z., Keppens R., 2009, ApJ, 705, 1594
Meliani Z., Keppens R., Giacomazzo B., 2008, A&A, 491, 321
Mignone A., Rossi P., Bodo G., Ferrari A., Massaglia S., 2010, MNRAS, 402, 7
Monceau-Baroux R., Keppens R., Meliani Z., 2012, A&A, 545, A62
Perucho M., Quilis V., Martí J.-M., 2011, ApJ, 743, 42
Porth O., Fendt C., 2010, ApJ, 709, 1100
Prokhorov D. A., Moraghan A., Antonuccio-Delogu V., Silk J., 2012, MNRAS, 425, 1753
Pushkarev A. B., Kovalev Y. Y., Lister M. L., Savolainen T., 2009, A&A, 507, L33
Rafferty D. A., McNamara B. R., Nulsen P. E. J., 2008, ApJ, 687, 899
Refaelovich M., Soker N., 2012, ApJ, 755, L3
Reynolds C. S., Fabian A. C., Celotti A., Rees M. J., 1996, MNRAS, 283, 873
Rosen A., Hughes P. A., Duncan G. C., Hardee P. E., 1999, ApJ, 516, 729
Schawinski K., Thomas D., Sarzi M., Maraston C., Kaviraj S., Joo S.-J., Yi S. K., Silk J., 2007, MNRAS, 382, 1415
Scheuer P. A. G., 1974, MNRAS, 166, 513
Sijacki D., Springel V., Di Matteo T., Hernquist L., 2007, MNRAS, 380, 877
Smith D. A., Wilson A. S., Arnaud K. A., Terashima Y., Young A. J., 2002, ApJ, 565, 195
Soker N., Akashi M., Gilkis A., Hillel S., Papish O., Refaelovich M., Tsebrenko D., 2012, arXiv:1209.0168
Sol H., Pelletier G., Asseo E., 1989, MNRAS, 237, 411
Synge J. L., 1957, The Relativistic Gas. North-Holland Pub. Co.
van Eerten H. J., Leventis K., Meliani Z., Wijers R. A. M. J., Keppens R., 2010, MNRAS, 403, 300
Wagner A. Y., Bicknell G. V., Umemura M., 2012, ApJ, 757, 136
Wardle J. F. C., Homan D. C., Ojha R., Roberts D. H., 1998, Nature, 395, 457

This paper has been typeset from a TEX/ LATEX file prepared by the author.

APPENDIX A: PASSIVE SCALAR ADVECTION: THE TRACING OF A CONSTITUENT

A tracer $\theta(t, \boldsymbol{r})$ that is transported along flow lines can only change under the influence of diffusivity and external sources such as

gravitation. In the case of ideal hydrodynamics and in the case where there is no diffusivity (apart from numerical effects which are small), a tracer is passively advected. In this case the tracer satisfies the equation:

$$\frac{d\theta}{dt} = \partial_t\theta + \boldsymbol{v}\cdot\nabla\theta = 0\ . \tag{A1}$$

By assigning different tracer values to various constituents of the flow, one can distinguish these constituents even in a complex flow geometry. The advection equation for the mass-density (the continuity equation) reads:

$$\partial_t D + \nabla\cdot(\boldsymbol{v}\,D) = 0\ . \tag{A2}$$

Since MPI-AMRVAC uses the conservative formulation of the fundamental equations (1), we use a conservative tracer equation. To that end we define:

$$\tilde{\theta}(t,\boldsymbol{r}) = \theta(t,\boldsymbol{r})\,D(t,\boldsymbol{r})\ . \tag{A3}$$

By writing out (A1) in terms of the rescaled tracer $\tilde{\theta}(t,\boldsymbol{r})$ and making use of the continuity equation (A2), the tracer advection equation can be written as:

$$\partial_t\tilde{\theta} + \nabla\cdot(\tilde{\theta}\,\boldsymbol{v}) = 0\ , \tag{A4}$$

hence, the rescaled tracer equation is in conservative form. MPI-AMRVAC will advect this rescaled tracer as a regular flux variable. To obtain the actual tracer we substitute back

$$\theta(t,\boldsymbol{r}) = \frac{\tilde{\theta}(t,\boldsymbol{r})}{D(t,\boldsymbol{r})}\ . \tag{A5}$$

We choose $\tilde{\theta}(t,\boldsymbol{r})$ to lie in the range

$$-D(t,\boldsymbol{r}) \leqslant \tilde{\theta} \leqslant +D(t,\boldsymbol{r})\ . \tag{A6}$$

The original tracer will then lie in the range

$$-1 \leqslant \theta(t,\boldsymbol{r}) \leqslant +1\ . \tag{A7}$$